Universidade Estadual de Campinas
Instituto de Física Gleb Wataghin

Allan Cassio Trevelin Covacevice

Modulação de microcavidades ópticas planares por ondas acústicas de superfície

Modulation of planar optical microcavities by surface acoustic waves

campinas
2015

Allan Cassio Trevelin Covacevice

Modulação de microcavidades ópticas planares por ondas acústicas de superfície

Modulation of planar optical microcavities by surface acoustic waves

Dissertação apresentada ao Instituto de Física "Gleb Wataghin" da Universidade Estadual de Campinas como parte dos requisitos exigidos para a obtenção do título de Mestre em Física.

Dissertation presented to the Institute of Physics "Gleb Wataghin" of the State University of Campinas in partial fulfillment of the requirements for the degree of Master in the area of Physics.

Supervisor/Orientador: ODILON DIVINO DAMASCENO COUTO JÚNIOR

ESTE EXEMPLAR CORRESPONDE À VERSÃO FINAL DA DISSERTAÇÃO DEFENDIDA PELO ALUNO ALLAN CASSIO TREVELIN COVACEVICE, E ORIENTADA PELO PROF. DR. ODILON DIVINO DAMASCENO COUTO JÚNIOR.

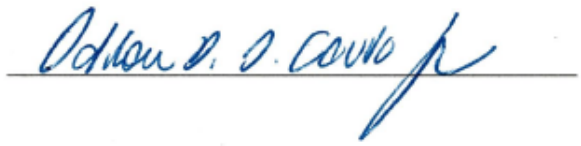

CAMPINAS
2015

Agência de fomento: Capes
Nº processo: 2013/118635-2

Ficha catalográfica
Universidade Estadual de Campinas
Biblioteca do Instituto de Física Gleb Wataghin
Valkíria Succi Vicente - CRB 8/5398

Covacevice, Allan Cassio Trevelin, 1989-
C837m Modulation of planar optical microcavities by surface acoustic waves / Allan Cassio Trevelin Covacevice. – Campinas, SP : [s.n.], 2015.

Orientador: Odilon Divino Damasceno Couto Júnior.
Dissertação (mestrado) – Universidade Estadual de Campinas, Instituto de Física Gleb Wataghin.

1. Ondas acústicas superficiais. 2. Microcavidades ópticas. 3. Modulação acusto-óptica. 4. Simulação computacional. I. Costa Júnior, Odilon Divino Damasceno,1979-. II. Universidade Estadual de Campinas. Instituto de Física Gleb Wataghin. III. Título.

Informações para Biblioteca Digital

Título em outro idioma: Modulação de microcavidades ópticas planares por ondas acústicas de superfície
Palavras-chave em inglês:
Surface acoustic waves
Optical microcavities
Acousto-optic modulation
Computational simulation
Área de concentração: Física
Titulação: Mestre em Física
Banca examinadora:
Odilon Divino Damasceno Couto Júnior [Orientador]
Maurício Morais de Lima Júnior
Paulo Clóvis Dainese Júnior
Data de defesa: 28-08-2015
Programa de Pós-Graduação: Física

MEMBROS DA COMISSÃO JULGADORA DA DISSERTAÇÃO DE MESTRADO DE **ALLAN CASSIO TREVELIN COVACEVICE – RA 085738** APRESENTADA E APROVADA AO INSTITUTO DE FÍSICA "GLEB WATAGHIN", DA UNIVERSIDADE ESTADUAL DE CAMPINAS, EM 28 / 08 / 2015.

COMISSÃO JULGADORA:

Prof. Dr. Odilon Divino Damasceno Couto Júnior - Orientador do Candidato
DFMC/IFGW/UNICAMP

Prof. Dr. Maurício Morais de Lima Júnior – ICM/UV - Espanha

Prof. Dr. Paulo Clóvis Dainese Júnior – DEQ/IFGW/UNICAMP

Agradecimentos

Agradeço à minha família pelo apoio, amor e dedicação.

Aos meus amigos, pela companhia insubstituível e boas cervejas.

Ao meu orientador, pelos ensinamentos e pela paciência.

À CAPES (2013/118635-2) e à Fapesp (2012/11382-9) pelo apoio financeiro.

Resumo

Neste trabalho, implementamos cálculos feitos através do método de elementos finitos no estudo de propriedades mecânicas e ópticas de microcavidades ópticas planares (POMCs) quando estas estão sob os efeitos de modulação induzidos por ondas acústicas de superfície (SAWs). Começamos resolvendo separadamente os problemas de modulação mecânica e caracterização de modos ópticos. Após isso, fundimos esses dois modelos em um terceiro, permitindo a caracterização da modulação acusto-óptica do sistema, o que nos permite também calcular as alterações induzidas nas propriedades ópticas das POMCs devido às SAWs.

Concentramos nossa atenção em POMCs que possuem refletores de Bragg (DBRs) compostos por camadas de materiais fortemente piezoelétricos, como o ZnO e o $LiNbO_3$. Mostramos que, usando em torno de 10 DBRs acima e abaixo da cavidade óptica, POMCs baseadas em ZnO/SiO_2 e $LiNbO_3/SiO_2$ poderiam, em princípio, apresentar fatores de qualidade excedentes a 10^4. O alto confinamento de luz na cavidade permite-nos observar efeitos relacionados ao forte acoplamento fóton-fônon induzido pelas SAWs. Em particular, mostramos como a presença de SAWs confere a formação de super-redes ópticas dinâmicas induzidas acusticamente, as quais são caracterizadas pela dobradura ("folding") da dispersão dos fótons na cavidade, e pelo surgimento de "mini" zonas de Brillouin. Nossos resultados estão de acordo com resultados experimentais presentes na literatura. Eles abrem a possibilidade de caracterização de modulações acusticamente induzidas em sistemas de camadas arbitrários e criam uma plataforma muito boa para interpretação de resultados experimentais.

Palavras-chave: ondas acústicas de superfície, microcavidades ópticas planares, modulação acusto-óptica, simulação computacional.

Abstract

In this work, we implement finite element method calculations to study the mechanical and optical properties of planar optical microcavities (POMCs) under the strain modulation induced by surface acoustic waves (SAWs). We start by solving separately the problems of mechanical modulation and optical mode characterization. Afterwards, we merge the two models in a single one which enables the characterization of the acousto-optic modulation in the system and allows us to calculate the SAW induced modification in the optical properties of POMCs.

We concentrate our attention in POMCs which have distributed Bragg reflectors (DBRs) composed of layers of highly piezoelectric materials like ZnO and $LiNbO_3$. We show that, using around 10 DBRs on top and below the optical cavity layer, POMCs based on ZnO/SiO_2 and $LiNbO_3/SiO_2$ could, in principle, have Q-factors exceeding 10^4. The strong light confinement in the cavity allows us to the observe effects related to the strong photon-phonon coupling induced by the SAW. In particular, we show how the presence of SAWs leads to the formation of acoustically induced dynamic optical superlattices, which are characterized by the folding of photon dispersion in the cavity and the appearance of "mini" Brillouin zones. Our results are in very good agreement with experimental results reported in literature. They open the possibility of characterization of acoustically induced modulation in arbitrary layered systems and create a very good platform for interpretation of experimental results.

Keywords: surface acoustic waves, planar optical microcavities, acousto-optic modulation, computational simulation.

"Praise be to the light. You have accomplished the impossible (...)"

- Tyrael, the Archangel.

Contents

Chapter 1

Introduction

This introductory chapter describes our main motivations to study the modulation of planar optical microcavities (POMCs) using surface acoustic waves (SAWs). In the first two sections, we give an overview about the research being currently done using SAWs and POMCs independently. In the third one, we explain why to study their coupling. In section 1.4, we spend a few words about the methodology used to achieve our main goals.

1.1 Surface acoustic waves

SAWs are usually generated on piezoelectric substrates using *interdigital transducers* (IDTs) [1, 2] via the *converse piezoelectricity* effect [3, 4]. Besides their common technological applications which date from the 60's [5], SAWs have called the attention in fundamental science applications in the recent few decades. In semiconductor nanostructures in special, the SAW strain and piezoelectric fields have been employed in a variety of experiments which involve carrier [6], spin [7, 8, 9] and exciton [10, 11] transport in quantum wells. In quantum dots, it has also been used to control the generation of single photon sources [12].

The ability to predict SAW modes and calculate their main mechanical and electrical properties in planar structures is, therefore, very important either in order to understand qualitative and quantitative experimental results or to predict the mechanical behavior of a desired material architecture. To realize this task in a successful way was one of our main goals in this work. In chapter 2, we demonstrate how to achieve it using Finite Element Method (FEM) calculations.

1.2 Planar optical microcavities

In the past several decades, light-matter interactions have received increasing attention by the scientific community [13, 14, 15, 16]. Not just for innate interest in the fundamentals of

physical and material sciences, but also due to the growing demand for efficient, faster and cheaper technologies for transmission and storage of information, filtering and sensing.

Here, we study POMCs, which are a particular photonic structure generally used to achieve strong light-matter coupling. POMCs are layered planar structures capable of confining photons to a tiny region: the optical cavity layer. Light confinement is realized by using a large number of material layers with contrasting refractive indexes (called Bragg mirrors (BMs)) which sandwich the optical cavity [17, 18]. Such devices are also known as 1D photonic crystals [18], as their refractive index periodicity lies in only one direction. Applications of POMCs involve, for example the enhancement of light emission from nanostructures (i.e., quantum wells, quantum dots, nanowires) inside the optical cavity [19, 20].

Another goal of this work is to be able to design POMCs composed of arbitrary material layers, which resonate in the visible/infrared spectral regions. In chapter 3, we show how employ FEM to calculate the main optical properties of this type of photonic structure which could be used in the future in light-matter coupling experiments.

1.3 Acousto-optic modulation

Due to the acousto-optic effect [1, 18, 21, 22], SAWs are capable of inducing changes to the dielectric properties of solids [23]. Since SAWs can be controlled by electrical means, they can be used as powerful instruments to tune the mechanical and optical properties of POMCs. This has been successfully realized in POMCs composed of III-V semiconductor heterostructures which are based on AlGaAs compounds. In such systems, very interesting experiments have been performed to demonstrate the formation of optical superlattices [24] and to study polariton dynamics [25, 26]. On the other hand, the use of III-V semiconductors, such as GaAs, in this type of experiment is not very much appropriate due to their weak piezoelectricity. In POMCs, the enhanced photon confinement requires a larger number of BMs, so the amplitude of SAW fields achieved in the optical cavity is limited to the penetration depth of the SAW in the material. One way to overcome this limitation would be to design POMCs where Bragg mirror layers are composed of strongly piezoelectric materials. Another advantage of moving away from GaAs structures would also be the possibility of working with CMOS compatible structures. Therefore, new materials must be proposed, tested (via simulations) and reproduced in experiments.

The study of structures which create this perspective is the main goal of this work. In chapter 4, we focus our attention on the acousto-optic modulation of highly piezoelectric POMCs with BMs composed of ZnO or Z-cut $LiNbO_3$ layers. By merging our separate SAW and POMCs models, we are able to predict the optical response of a POMC when a SAW is propagating. We show how the strong photon-phonon interaction leads to the formation of dynamic optical

superlattices (characterized by the acoustic wavelength) and demonstrate how the formation of these superlattices leads to the folding of the photon dispersion, in very good agreement with experimental results obtained for GaAs/AlGaAs based POMCs [24, 27].

1.4 Methodology

This work makes use of COMSOL Multiphysics, which is an integrated simulation platform that computationally solves physics problems via the *finite element method* (FEM) [28] - a numerical solver that discretizes the simulation geometry into many tiny elements (the finite elements, or *mesh*, as shown in Figure 1.1). Numerical solutions to physical equations are then achieved in each of these elements by matrix factorization methods, where more finite elements means better data convergence. The main reason for working with numerical solutions is that we are very much interested in learning more about COMSOL, as it consists of a powerful tool that will eventually allow for the simulation of even more complex structures.

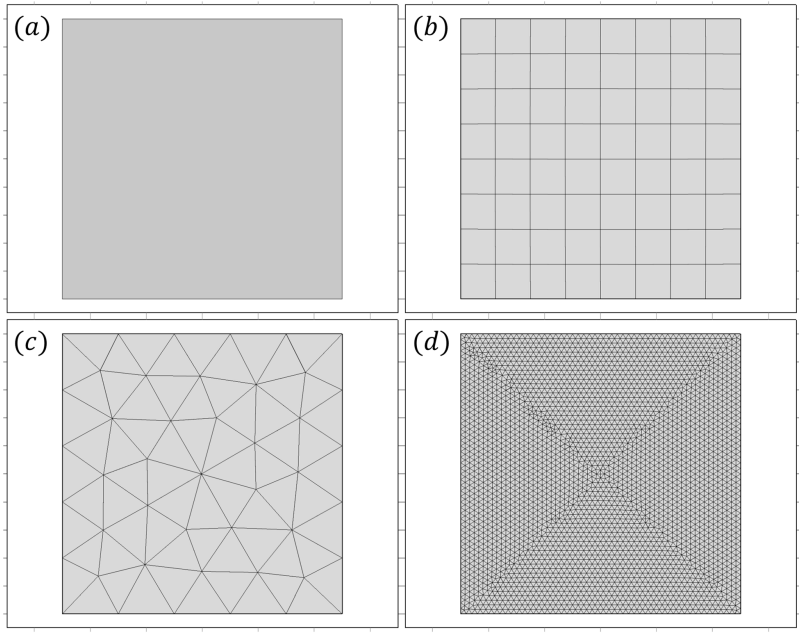

Figure 1.1: examples of the geometry discretization performed by the FEM. (a) Geometric sample in the absence of discretizations; (b) coarse quadricular mesh; (c) coarse triangular mesh; (d) fine triangular mesh.

Both SAW and POMC models can be simplified as two-dimensional (2D) problems. This requires much less computational effort than a full 3D solution would. Also, COMSOL allows us to merge two different problems in a single one. While the SAW problem scales in the 5-10μm range, the POMC one scales in the 500-800 nm range. We can unify these different scale problems and solve them in an independent or in a coupled way by using COMSOL.

Chapter 2

Surface acoustic waves in solids

2.1 Introduction

This chapter introduces the concept of surface acoustic waves (SAWs) propagating in solid media. We begin by introducing the theories of elasticity and the wave equation for non-piezoelectric solids. Later on, we will introduce the piezoelectricity mechanism and look into the wave equation for piezoelectric solids. We describe the particular solution of a Rayleigh SAW, on which this work is focused, and discuss about SAW generation. Finally, the last section is dedicated to the simulation model of Rayleigh SAWs propagation in piezoelectric solids.

2.2 Acoustic waves in non-piezoelectric solids

We refer to solids as arrays of tightly bonded atoms which are organized in specific periodic structures. Here, we explore the physical quantities involved and formulate the equation that describes wave propagation in such media.

2.2.1 Strain

When acoustic waves propagate in solids, they transfer energy to the atoms of the medium, causing these to oscillate, that is, to displace themselves from their equilibrium positions. This leaves the solid stressed and, in order to surpass this stress and remain in the minimum energy state, the solid undergoes a deformation: the *strain*.

The displacement vector of any infinitesimal volumetric portion of the solid can be defined as [5, 29]

$$\vec{u}(r) = \vec{r} - \vec{r}_0, \tag{2.1}$$

where $\vec{r}_0$ is the equilibrium positon vector in the global coordinate system. For a plane wave

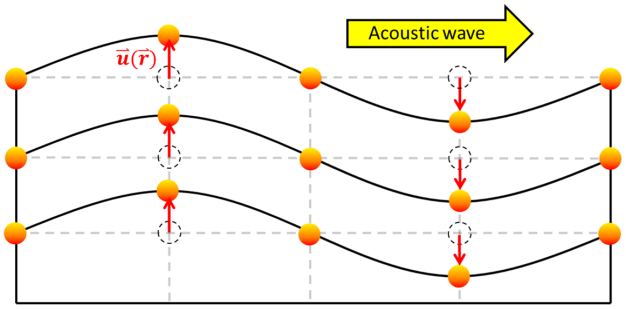

Figure 2.1: representation of the displacement vector (red) for atoms in a solid under acoustic wave propagation. The orange-filled circles represent the atoms, while the black-dashed circles represent their equilibrium positions in an unperturbed crystal lattice (gray grid).

disturbance, equation 2.1 can be written as [5]

$$\vec{u}(r,t) = (u_x\hat{x} + u_y\hat{y} + u_z\hat{z})e^{i(\vec{k}.\vec{r}-\omega t)}, \tag{2.2}$$

where u_x, u_y and u_z represent amplitudes (in units of length) in the three cartesian coordinates, $\vec{k}$ is the wave vector and ω is the angular frequency. Figure 2.1 is a representation of the displacement vector (red arrows) for atoms in a solid that are oscillating transversely to the direction of propagation of the wave.

Unidimensional description

In order to understand how the displacement vector is related to the strain, we introduce a simple one-dimensional example: an extensible string fixed in one end to a rigid wall while the other end is being pulled towards the right by a force $\vec{F}$. On the upper part of Figure 2.2, the string is unstressed and its initial length is L. When a force $\vec{F}$ pulls the string towards the right (bottom part of Figure), it becomes deformed to a length $L + \Delta L$. The unstressed string points M and N are located at their respective equilibrium positions x and $x + \Delta x$.

The stress due to $\vec{F}$ causes M and N to be displaced to points M' and N', located in x' and $x' + \Delta x'$, respectively. Thus, we have the following displacement vectors for points M and N

$$M : u(x) = x' - x; \tag{2.3a}$$
$$N : u(x + \Delta x) = (x' + \Delta x') - (x + \Delta x), \tag{2.3b}$$

where we have omitted the vectorial notation for simplicity. Equation 2.3b gives

$$u(x + \Delta x) = (x' - x) + (\Delta x' - \Delta x); \tag{2.3c}$$
$$= u(x) + \Delta u(x). \tag{2.3d}$$

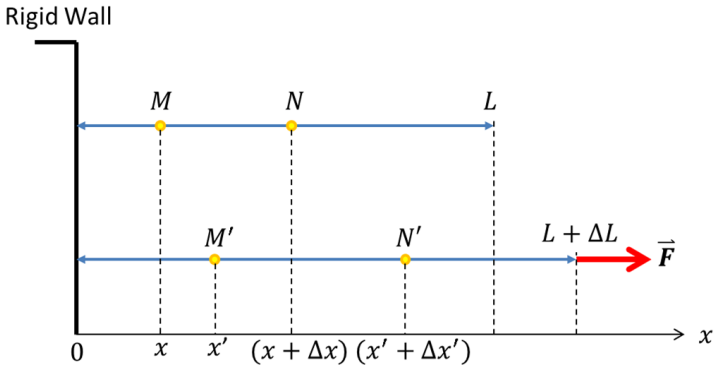

Figure 2.2: an extensible string that is fixed to a rigid wall on the left end is being pulled towards the right. It undergoes deformation, increasing its length from L to $L + \Delta L$. On top, the string is unstressed and the points M and N, which are located in x and $x + \Delta x$, respectively, were highlighted. On the bottom, the string is stressed by the application of an external force $\vec{F}$, which causes the points M and N to be displaced to points M' (located in x') and N' (located in $x' + \Delta x'$), respectively.

Equation 2.3d states that, if $\Delta u(x) \neq 0$, then the segment $\overline{MN}$ is deformed. Otherwise, it is just translated. Assuming that deformation occurs, the relative deformation is

$$\frac{\Delta L}{L} = \frac{u(x + \Delta x) - u(x)}{\Delta x}, \tag{2.4}$$

where L is the length of the segment. But $\overline{MN}$ might as well be very small, such as the distance between two atoms, so that we define strain as the limit

$$S \equiv \lim_{\Delta x \to 0} \frac{u(x + \Delta x) - u(x)}{\Delta x} = \frac{du(x)}{dx}. \tag{2.5}$$

Three-dimensional description

The presented example assumes the string to be perfectly unidimensional, more like a linear chain of atoms. A three-dimensional solid allows for the displacement to occur in all three directions, but that comes with mixed terms, that is, deformation in one direction provides deformations in the other directions as well. This suggests that strain is not a vector, but rather a second-rank tensor. Represented by a 3×3 matrix, this second-rank tensor is given by [29]:

$$S_{ij} = \frac{\partial u_i}{\partial x_j}, \quad \text{with } i, j = 1, 2, 3. \tag{2.6}$$

From now on, we associate spatial coordinates to the indexes 1, 2 and 3 as: $x \to x_1$, $y \to x_2$ and $z \to x_3$. The solid is deformed when the gradient from equation 2.6 is non-zero, that is,

$$\frac{\partial u_i}{\partial x_j} \neq 0. \tag{2.7}$$

Equation 2.6, however, is not adequate for the strain, and condition 2.7 alone is not sufficient to attest that deformation is occuring. Suppose we rotated the whole solid by a tiny angle $\alpha \approx 0$ about the Ox_3 axis. The new coordinates for atoms located at their equilibrium positions, x_j, are then given by equation 2.8:

$$x_i' = R_{ij}x_j, \tag{2.8}$$

where R_{ij} is the rotation matrix around Ox_3:

$$R_{ij} = \begin{bmatrix} \cos\alpha & \sin\alpha & 0 \\ -\sin\alpha & \cos\alpha & 0 \\ 0 & 0 & 1 \end{bmatrix} \approx \begin{bmatrix} 1 & \alpha & 0 \\ -\alpha & 1 & 0 \\ 0 & 0 & 1 \end{bmatrix}, \tag{2.9}$$

and the displacement of each atom would be

$$u_i = x_i' - x_i; \tag{2.10a}$$

$$u_i = R_{ij}x_j - x_i. \tag{2.10b}$$

Differentiating equation 2.10b with respect to x_j gives:

$$\frac{\partial u_i}{\partial x_j} = (R_{ij} - \delta_{ij}I), \tag{2.10c}$$

where δ_{ij} is the Kronecker delta and I is the identity matrix. Thus, rotation by a tiny angle α about the Ox_3 axis provides

$$\frac{\partial u_i}{\partial x_j} = \begin{bmatrix} 0 & \alpha & 0 \\ -\alpha & 0 & 0 \\ 0 & 0 & 0 \end{bmatrix} \neq 0. \tag{2.11}$$

Therefore, equation 2.6 accounts for the rotation of the solid as well, which must be subtracted. That can be arranged by taking the symmetric part of the gradient from equation 2.6, so we define strain as

$$S_{ij} = \frac{1}{2}\Big(\frac{\partial u_i}{\partial x_j} + \frac{\partial u_j}{\partial x_i}\Big). \tag{2.12}$$

Strain is a dimensionless physical quantity expressed by a symmetric second-rank tensor. It represents the deformation of a solid relatively to its original configuration.

2.2.2 Stress

A deformed solid experiences traction forces that tend to restore mechanical equilibrium. These forces arise from the interaction between neighbouring particles, being transmitted progressively through the solid by interatomic forces. The mechanical traction vector, $\vec{T}$, is defined

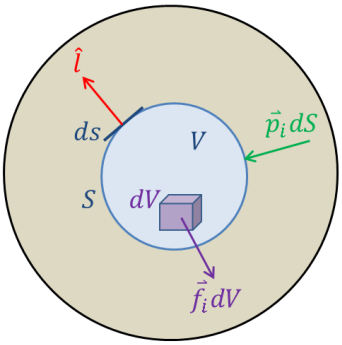

Figure 2.3: mechanical equilibrium of a volume within the solid. The material volume V is subjected to external surface forces with density $\vec{p_i}$ (green), and it responds with internal volumetric forces with density $\vec{f_i}$ (purple).

as the force per unit area exerted by a certain material volume on its neighbours through planes that separate them. In order to define the direction of the force, we define the unit vector $\hat{l} = (l_1, l_2, l_3)$, which is always normal to the surface element ds, as in Figure 2.3. Thus, $\vec{T}$ is directed in the opposite direction of $\hat{l}$, but they are not necessarily antiparallel, as shear forces can arise. The traction can be written as [29]

$$\vec{T}(\hat{l}) = \lim_{\Delta s \to 0} \frac{\Delta \vec{F}}{\Delta s} = \frac{d\vec{F}}{ds}. \tag{2.13}$$

In order to define mechanical stress, we state the equilibrium conditions inside a volume V subjected to external forces per unit area with density p_i, and internal forces per unit volume with density f_i, as shown in Figure 2.3 [29].

The total forces acting on the volume V is, therefore, the sum of the mechanical tractions on its surface and the restoring volumetric forces acting in its interior, so that

$$F_i = \int_s T_i(\hat{l}) ds + \int_V f_i dV = 0. \tag{2.14}$$

According to the Divergence Theorem in tensor notation [29, Appendix C],

$$\int_s A_i ds_j = \int_s A_i l_j ds = \int_V (\nabla_j . A_i) dV, \tag{2.15}$$

where A_i is an arbitrary-rank tensor and $ds_j = l_j ds$, with l_j being components of the unit vector normal to the surface. Equations 2.14 and 2.15 gather to obtain

$$f_i = -\sum_{j=1}^{3} \frac{\partial T_{ij}}{\partial x_j}, \tag{2.16a}$$

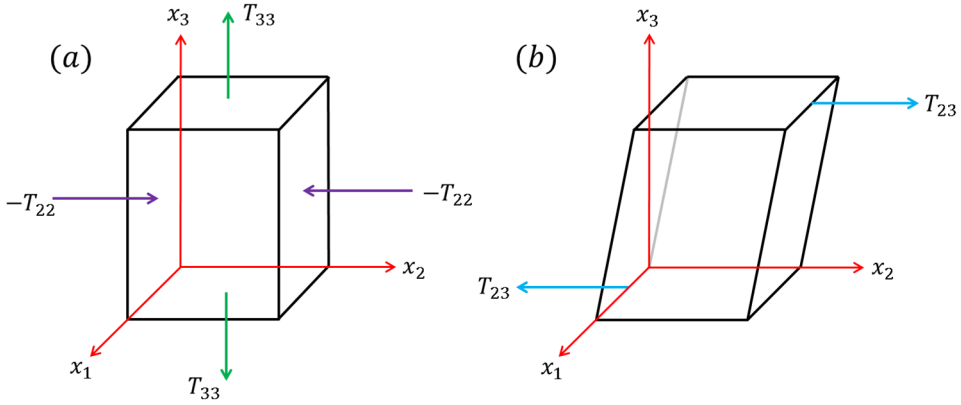

Figure 2.4: examples of compressional, tractional and shear components of the stress tensor. In 2.4(a), the T_{22} components (purple arrows) are compressing the solid, while the T_{33} components (green arrows) are tractioning it. In 2.4(b), the blue arrows represent the shear forces corresponding to the tangential component T_{23} of the stress tensor.

and

$$T_i(\hat{l}) = T_{ij} l_j, \tag{2.16b}$$

where $i, j = 1, 2, 3$. Equation 2.16b expresses the mechanical traction $\vec{T}(\hat{l})$ on a surface with any orientation $\hat{l}$ in terms of the quantities T_{ij} called *stresses* [29]. The stress tensor notation, T_{ij}, represents the i^{th} component of the force acting per unit area (units of N/m^2) on a surface perpendicular to the Ox_j axis, that is,

$$T_{ij} = \lim_{\Delta s_j \to 0} \frac{\Delta F_i}{\Delta s_j} = \frac{d\vec{F}_i}{ds_j}. \tag{2.17}$$

These nine quantities constitute the second-rank stress tensor, which is symmetric (the proof is presented in the Appendix), reducing the number of independent elements from nine to six.

Figure 2.4 shows some examples of compressional, tractional and shear components of the stress tensor. In practice, the stress tensor is not always symmetric (for example, when a polar crystal is subjected to an electric field), but this approximation is valid for practical purposes, because the external torque due to such mechanisms is often very weak [29].

(*i*) T_{11}, T_{22} and T_{33}: stresses normal to surfaces, corresponding to tractions or compressions;

(*ii*) T_{12}, T_{13} and T_{23}: tangential stresses, corresponding to shear forces.

2.2.3 Hooke's law in three dimensions

A solid is said to be elastic when it completely restores its initial shape after an external stress is applied and then removed. Experimental evidence shows that, for small deformations, the elastic behaviour of most solids is well described by the first-order term in the following Taylor expansion [29]:

$$T_{ij}(S_{kl}) = T_{ij}(0) + S_{kl}\left(\frac{\partial T_{ij}}{\partial S_{kl}}\right)_{S_{kl}=0} + \frac{S_{kl}S_{mn}}{2}\left(\frac{\partial^2 T_{ij}}{\partial S_{kl}\partial S_{mn}}\right)_{S_{kl}=S_{mn}=0} + \dots \tag{2.18}$$

where summation over the dummy indexes $(k, l, m, n...)$, from 1 to 3, is implied. Expliciting this summation and, since $T_{ij}(0) = 0$, we obtain

$$T_{ij} = \sum_{k,l=1}^{3} c_{ijkl} S_{kl}, \tag{2.19}$$

where we define

$$c_{ijkl} \equiv \left(\frac{\partial T_{ij}}{\partial S_{kl}}\right)_{S_{kl}=0}. \tag{2.20}$$

Equation 2.19 is the Hooke's law in three dimensions. Analogously to the unidimensional case, it relates the deformation of a solid (strain) to the applied force (stress) through an elastic constant. The term c_{ijkl}, is a fourth-rank tensor known as the stiffness tensor. It physically represents the spring constant of a three-dimensional solid, and it is related to the solid's cristalline structure. Its units are usually expressed in N/m^2.

The stiffness tensor may seem quite complicated, as it contains $3^4 = 81$ elements, but since both stress and strain tensors are symmetric, the stiffness tensor becomes invariant when interchanging the first or last two indexes: $c_{ijkl} = c_{jikl}$ and $c_{ijkl} = c_{ijlk}$. This reduces the number of independent constants from 81 to 36, allowing for the following simplified notation [5]:

$$T_I = \sum_{J=1}^{6} c_{IJ} S_J, \tag{2.21}$$

where we have reduced the number of indexes according to Table 2.1. Equation 2.21 is the three-dimensional Hooke's law in reduced notation (also known as *engineering notation*). The stiffness tensor becomes even more simple due to the symmetries of crystals: depending on the crystalline structure of the material, many elements of its matrix representation are either null or equal to others [30]. Table A.1 from Appendix shows unit cells and stiffness tensors for cubic, hexagonal and trigonal crystalline structures, while Table A.2 exhibits some mechanical properties for several materials of our interest.

Index ij	Reduced index I	Matrix representation
11	1	
22	2	
33	3	$\begin{bmatrix} T_1 & T_6 & T_5 \\ T_6 & T_2 & T_4 \\ T_5 & T_4 & T_3 \end{bmatrix}$
23 or 32	4	
13 or 31	5	
12 or 21	6	

Table 2.1: indexes expressed in reduced notation.

2.2.4 The wave equation for non-piezoelectric solids

We now consider the unidimensional spring-mass problem, as depicted by Figure 2.5:

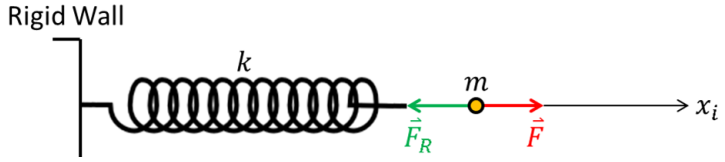

Figure 2.5: the unidimensional spring-mass system. A massless spring, with elastic constant k, has a mass m attached to its tip, which is being pulled towards the right by a force $\vec{F}$. An opposite force, $\vec{F}_R$, then appears to restore mechanical equilibrium.

The spring is assumed to be massless and its elastic constant is k. A mass m is attached to its tip and is being pulled towards the right by a force $\vec{F}$. A restoring force, $\vec{F}_R = -ku_i\hat{x}_i$, then appears in order to oppose the deformation and establish mechanical equilibrium.

Assuming there is no damping, Newton's second law for such a system when force $\vec{F}$ is released is

$$m\frac{d^2u_i}{dt^2} = -ku_i, \tag{2.22}$$

which is the equation of motion for the spring-mass system. In section 2.2.2, we expressed the restoring forces of a three-dimensional solid as

$$F_R = \int_V f_i dV, \tag{2.23}$$

where f_i is given by equation 2.16a.

Thus, in analogy to the unidimensional spring-mass problem, Newton's second law for a three-dimensional solid reads

$$m\frac{d^2u_i}{dt^2} = \sum_{j=1}^{3}\int_V \frac{\partial T_{ij}}{\partial x_j}dV. \tag{2.24}$$

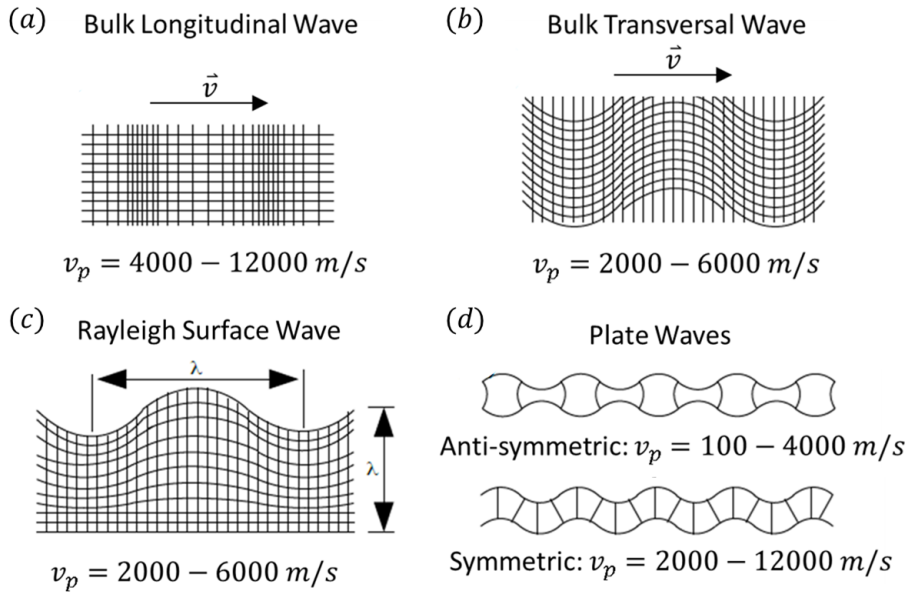

Figure 2.6: representation of elastic waves that propagate inside a solid towards the right. The displacements are exaggerated for better visualization, and typical wave velocities, v_p, are presented in each case. (a) Bulk longitudinal (compressional) wave in unbounded solid. (b) Bulk transversal (shear) wave. (c) Rayleigh SAW in semi-infinite solid, where wave motion extends below the surface to a depth of about one wavelength. (d) Waves in thin solid plates.

Since we are dealing with tiny portions of the solid, such as the size of atomic bonds, we have $V \to 0$. Therefore, the term $\partial T_{ij}/\partial x_j$ can be regarded as a constant in this region of integration, for it varies too slowly (if it even varies). Thus, equation 2.24 becomes

$$\rho \frac{d^2 u_i}{dt^2} = \sum_{j=1}^{3} \frac{\partial T_{ij}}{\partial x_j}, \tag{2.25}$$

where $\rho = m/V$ is density. Equation 2.25 is the equation of motion for three-dimensional solids. In fact, it is a set of three equations.

Equation 2.25 does not look like a wave equation, but stress can be written in terms of strains by using Hooke's law from equation 2.19:

$$\rho \frac{d^2 u_i}{dt^2} = \sum_{j,k,l=1}^{3} \frac{\partial}{\partial x_j}(c_{ijkl} S_{kl}). \tag{2.26}$$

Using the expression from equation 2.12 gives

$$\rho \frac{d^2 u_i}{dt^2} = \sum_{j,k,l=1}^{3} \frac{\partial}{\partial x_j}\left[\frac{c_{ijkl}}{2}\left(\frac{\partial u_k}{\partial x_l} + \frac{\partial u_l}{\partial x_k}\right)\right]. \tag{2.27}$$

But c_{ijkl} is invariant to exchanging the first or last two indexes, so that [29]

$$c_{ijkl}\frac{\partial u_l}{\partial u_k} = c_{ijlk}\frac{\partial u_l}{\partial u_k} = c_{ijkl}\frac{\partial u_k}{\partial u_l}. \tag{2.28}$$

Therefore, we obtain

$$\rho\frac{d^2u_i}{dt^2} = \sum_{j,k,l=1}^{3} c_{ijkl}\frac{\partial^2 u_l}{\partial x_j \partial x_k}. \tag{2.29}$$

This is the set of three wave equations for three-dimensional non-piezoelectric solids. It relates a second time-derivative of the displacement vector to its second spatial-derivative, and can completely describe the motion of acoustic waves in solids. Various types of such waves can occur depending on the properties of the solid and its boundaries. Figure 2.6 shows schematically the waves that can propagate in an unbounded solid, a semi-infinite solid having a single plane boundary, and a solid plane that has two plane boundaries [5].

2.3 Piezoelectricity

The piezoelectric effect was discovered by Jacques Curie and Pierre Curie as early as in 1880 [31]. It was observed that some solids, while in certain crystal cuts, would produce an electrification when under mechanical pressure. Eventually, the converse piezoelectricity, i.e., a deformation or stress due to an external electric field, was mathematically deduced from the fundamental principles of thermodynamics by Lippmann in 1881 [3], which was later experimentally observed by the Curie brothers [4].

2.3.1 The piezoelectric constitutive relations

The term *piezoelectricity* describes the ability of certain materials to develop an electric displacement field, $\vec{D}$, that is proportional to an applied stress and, consequently, to the strain. The electric charges present on the electrodes reverses their sign if the stress changes from tensile to compressive (Figure 2.7(a)). Since all piezoelectric materials present the converse effect, they deform under applied electric field (blue arrows) and the sign of the strain changes to the opposite one if one reverses the direction of the electric field, $\vec{E}$ (Figure 2.7(b)).

In direct piezoelectricity, the solid becomes polarized as a response to the mechanical stress. This polarization produces a piezoelectric field, $\vec{E}_k$ (purple arrows in Figure 2.7), in order to oppose the stress and restore mechanical and electrical equilibrium. In converse piezoelectricity, this field tries to cancel the external electric field inside the solid.

The theories of elasticity and piezoelectricity provide a description for the motion of acoustic waves inside piezoelectric solids. The elastic constitituve relations for a dielectric, non-

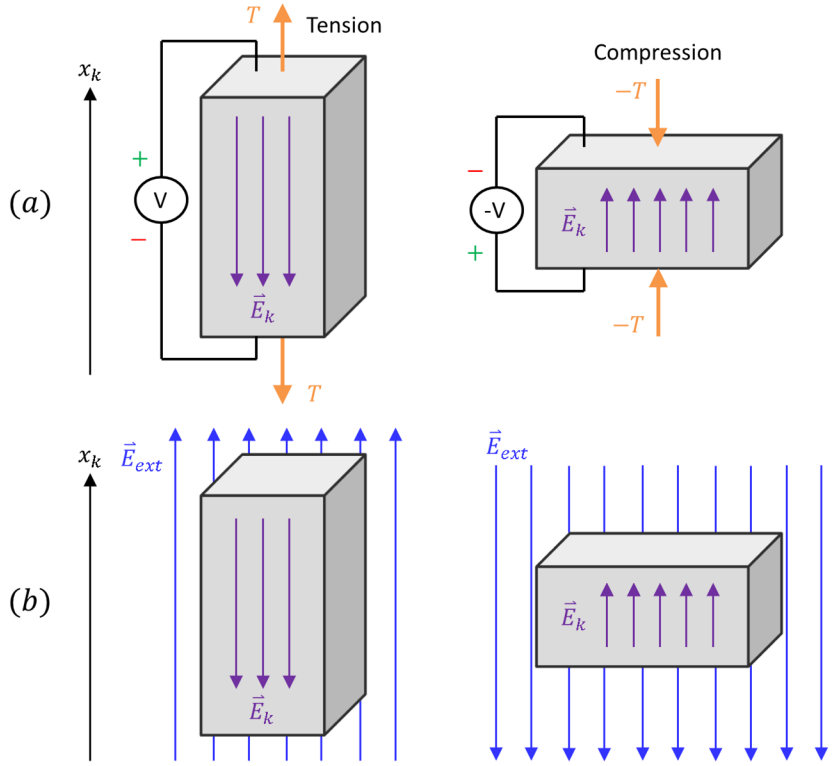

Figure 2.7: schematic representation of the longitudinal (a) direct and (b) converse piezoelectric effects. In (a), tensioning the piezoelectric crystal is inducing the appearance of a certain voltage, V, on the voltimeter. When the stress goes from tensile to compressive, however, this voltage turns to $-V$. This has been observed to be equivalent to the application of an external electric field, $\vec{E}_{ext}$ to the solid, as in Figure (b).

piezoelectric solid are given by equations 2.30(a-b):

$$T_{ij} = c^E_{ijkl} S_{kl}; \tag{2.30a}$$

$$D_k = \epsilon^T_{kl} E_l, \tag{2.30b}$$

where D_k is the electrical displacement field (vector, or first-rank tensor), ϵ_{kl} is the relative permittivity second-rank tensor. The upper indexes indicate that stiffness and relative permittivity values are measured at zero external electric fields and stresses.

Accounting for the piezoelectric effect, the set of equations 2.30 can be written as [5, 29]

$$T_{ij} = c^E_{ijkl} S_{kl} - d_{kij} E_k; \tag{2.31a}$$

$$D_k = \epsilon^T_{kl} E_l + d_{kij} S_{ij}, \tag{2.31b}$$

where E_k is the piezoelectric field (a vector, or first-rank tensor) and d_{kij} is the piezoelectric tensor (third-rank tensor), also known as the *coupling matrix*, in units of C/m^2. These equations are known as the *piezoelectric constitutive relations*, where summation over the dummy indexes,

from 1 to 3, is implied.

The number N of independent constants of a third-rank tensor may be as large as $3^3 = 27$. However, the piezoelectric tensor may have at most 18 of those, because $d_{kij} = d_{kji}$ due to the symmetry of the stress and strain tensors. For that reason, the piezoelectric tensor can also be written in reduced notation:

$$d_{kij} = d_{kI}, \tag{2.32}$$

where I is the same as in Table 2.1. Thus, the piezoelectric tensor is represented by a 3×6 matrix. The case where $N = 18$ corresponds to the triclinic crystals of class 1 [30]. In crystals with higher symmetry, this value decreases even more; for example, some cubic classes present $N = 1$. Table A.3 from the Appendix presents the piezoelectric tensors and constants for several materials of interest in this work.

The crystallographic symmetry of materials plays a decisive role in piezoelectricity. According to the definition of the piezoelectric effect, all components of the piezoelectric tensor should vanish in crystals possessing a center of symmetry. However, it represents a necessary but not sufficient requirement for a material to exhibit any sizeable piezoelectric effect [2].

2.3.2 The wave equation for piezoelectric solids

The wave equation for piezoelectric solids can be obtained by using equations 2.31a and 2.25:

$$\rho \frac{d^2 u_i}{dt^2} = \sum_{j=1}^{3} \frac{\partial T_{ij}}{\partial x_j} = \sum_{j=1}^{3} \frac{\partial (c^E_{ijkl} S_{kl})}{\partial x_j} - \sum_{j=1}^{3} \frac{\partial (d_{kij} E_k)}{\partial x_j}. \tag{2.33}$$

Assuming material properties to be constant, equation 2.33 becomes

$$\rho \frac{d^2 u_i}{dt^2} = \sum_{j,k,l=1}^{3} c^E_{ijkl} \Big(\frac{\partial^2 u_l}{\partial x_j \partial x_k} \Big) - \sum_{j=1}^{3} d_{kij} \Big(\frac{\partial E_k}{\partial x_j} \Big). \tag{2.34}$$

Noting that

$$E_k = -\Big(\frac{\partial \phi}{\partial x_k} \Big), \tag{2.35}$$

where ϕ is the piezoelectric potential, we obtain

$$\rho \frac{d^2 u_i}{dt^2} = \sum_{j,k,l=1}^{3} c^E_{ijkl} \Big(\frac{\partial^2 u_l}{\partial x_j \partial x_k} \Big) + \sum_{j,k=1}^{3} d_{kij} \Big(\frac{\partial^2 \phi}{\partial x_j \partial x_k} \Big). \tag{2.36}$$

This is the wave equation for piezoelectric solids. The comparison between equations 2.29 and 2.36 gives evidence of an additional term on the right side of the latter. As it contains the piezoelectric potential alone, it has become clear that piezoelectricity can impact the acoustic motion inside a solid. This suggests that acoustic waves can be generated by electrical means.

We shall now explore this a little further in order to introduce how SAWs can be generated.

2.3.3 SAW generation

The presence of piezoelectricity in certain materials allows for the generation of SAWs via its converse effect. This process makes use of devices known as *interdigital transducers* (IDTs), which are pairs of periodic, usually E-shaped electrodes deposited on the surface of piezoelectric substrates.

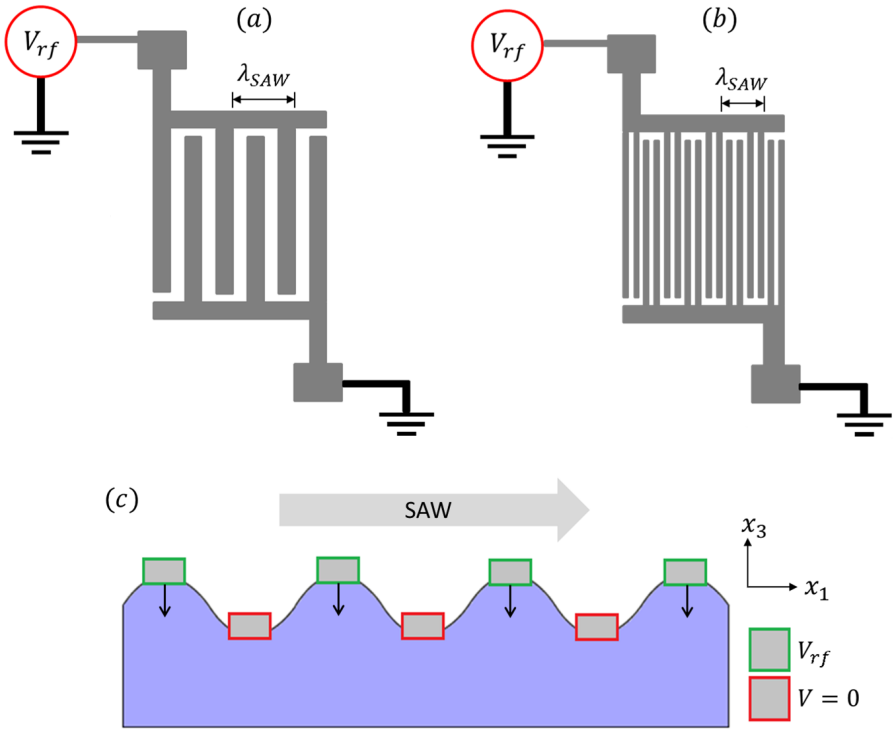

Figure 2.8: representations of (a) single-finger and (b) double-finger IDTs. Two pairs of E-shaped electrodes are intercalated by a distance $\lambda_{SAW}/4$ in (a) and $\lambda_{SAW}/8$ in (b), where λ_{SAW} is the SAW wavelength. (c) The RF potential (V_{rf}) applied between the IDTs is related to the SAW frequency (f_{SAW}) and amplitude. When $V_{rf}(f = f_{SAW})$, deformations on the substrate occur due to converse piezoelectricity effect, where the electrodes oscillate between wave crests and valleys, launching a SAW along x_1.

Figures 2.8(a-b) present two main types of IDTs: the single-finger (Figure 2.8(a)), and the double-finger IDT (Figure 2.8(b)). Several characteristics of the generated SAW, such as the wavelength (λ_{SAW}), are determined by construction of these devices, not being further tunable. Reference [2] presents several materials compatible with the IDT technology, as well as many design and fabrication techniques.

Applying a radio-frequency (RF) electric potential, $V_{rf}(f = f_{SAW})$, between the electrodes causes a strain field to appear on the substrate. As the applied potential reverses its sign,

so does the strain, and the electrodes oscillate between crests and valleys according to Figure 2.8(c), launching a SAW along the material surface.

The choice between single and double-finger IDTs lies in contouring experimental difficulties. The latter offers reduced acoustic reflections on the electrodes at the cost of being more challenging to be constructed [27]. There are also difficulties in collimating SAW beams, as these can spread out over the surface. In order to contour this, the use of waveguides and concave IDTs [27] offers great advantages.

2.3.4 The Rayleigh SAW in piezoelectric solids

A group of solutions to equation 2.29 is composed by acoustic waves which are restricted to propagate on the surface of solids and liquids, and which decay exponentially with the depth into the substrate. These waves present a linear dispersion relation where it is observable that SAW modes are usually slower than bulk modes. Thus, surface of solids act as waveguides, as the interface between the solid and air can be regarded as a "slow film" [27]. This allows for high acoustic energy densities in these regions, and ease in collimating SAW beams.

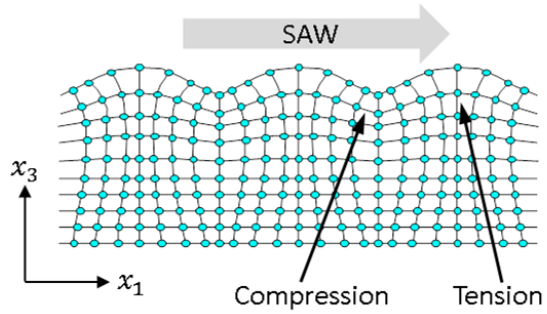

Figure 2.9: representation of Rayleigh SAW propagation in solids. Particles of the medium move in the x_1Ox_3 plane, with decaying amplitudes towards the depth of the solid. This movement creates regions of increased (compression) and decreased (tension) particle densities, ρ, in the near-surface region.

The Rayleigh wave is a particular case among the group of SAWs. Named after Lord Rayleigh, the man responsible for its prediction in 1885 [32], it consists of a coupling between longitudinal and transversal modes where the surface particles of a solid undergo elliptical displacement in a plane oriented perpendicularly to the wave vector, as in Figure 2.9.

In the near-surface region, the elliptic motion is retrograde (counterclockwise when the wave travels from left to right), while the particle motion becomes prograde at greater depths. In addition, the motion amplitude decays and the eccentricity changes as the depth increases. The depth of significant displacement in the solid is usually the order of magnitude of the acoustic wavelength, λ_{SAW}. For a Rayleigh SAW with wave vector $\vec{k}_{SAW} = (k, 0, 0)$, the semi-infinite model divides space in two domains: the region where $|x_3| > 0$ is filled with air, while region

$|x_3| < 0$ contains the solid. Therefore, we treat the surface as the plane x_1Ox_2 at $x_3 = 0$, and the elliptical displacement occurs in the x_1Ox_3 plane. The Rayleigh SAW is characterized by three important conditions:

$$\text{i) } \vec{u} = (u_1, 0, u_3) : \text{ purely longitudinal } (u_1) \text{ and transversal } (u_3) \text{ modes;} \tag{2.37a}$$

$$\text{ii) } |\vec{u}| \to 0 \text{ as } |x_3| \to \infty : \text{ amplitude decays with the depth of the substrate;} \tag{2.37b}$$

$$\text{iii) } T_{ij}(x_3 = 0) = 0 : \text{ the surface is stress-free.} \tag{2.37c}$$

Condition 2.37a omits the number 2 from the dummy indexes in equation 2.29, as no motion occurs in the x_2 direction. In reduced notation, the other two displacement components can be obtained by solving the following equations

$$\rho\frac{\partial^2 u_1}{\partial t^2} = \frac{\partial^2}{\partial x_1^2}(c_{11}u_1 + c_{15}u_3) + \frac{\partial^2}{\partial x_1 \partial x_3}[(c_{15} + c_{51})u_1 + (c_{13} + c_{55})u_3] + \frac{\partial^2}{\partial x_3^2}(c_{55}u_1 + c_{53}u_3), \tag{2.38a}$$

$$\rho\frac{\partial^2 u_3}{\partial t^2} = \frac{\partial^2}{\partial x_1^2}(c_{51}u_1 + c_{55}u_3) + \frac{\partial^2}{\partial x_1 \partial x_3}[(c_{55} + c_{31})u_1 + (c_{53} + c_{35})u_3] + \frac{\partial^2}{\partial x_3^2}(c_{35}u_1 + c_{33}u_3). \tag{2.38b}$$

The additional term in equation 2.36 contributes to equations 2.38a and 2.38b, respectively, with

$$d_{11}\frac{\partial^2 \phi}{\partial x_1^2} + (d_{15} + d_{31})\frac{\partial^2 \phi}{\partial x_1 \partial x_3} + d_{35}\frac{\partial^2 \phi}{\partial x_3^2}, \tag{2.39a}$$

$$d_{15}\frac{\partial^2 \phi}{\partial x_1^2} + (d_{13} + d_{35})\frac{\partial^2 \phi}{\partial x_1 \partial x_3} + d_{33}\frac{\partial^2 \phi}{\partial x_3^2}. \tag{2.39b}$$

The presence of mixed terms in equations 2.38(a-b) and 2.39(a-b) gives evidence of the coupling between the longitudinal and transversal modes. It is also noticeable that these equations are dependent on the crystalline structure of the solid, as well as the wave's direction of propagation.

The general solution to equations 2.38 and 2.39 for Rayleigh SAW propagation along x_1 in the x_1Ox_3 plane can be written as [33]

$$u_j = U_j \exp(-\alpha_j x_3) \exp[i(kx_1 - \omega t + \varphi_j)]; \tag{2.40a}$$

$$\phi = \phi_0 \exp(-\alpha_j x_3) \exp[i(kx_1 - \omega t)], \; j = 1, 3; \tag{2.40b}$$

where U_j and ϕ_0 are displacement and piezoelectric potential amplitudes, respectively, α_j is the

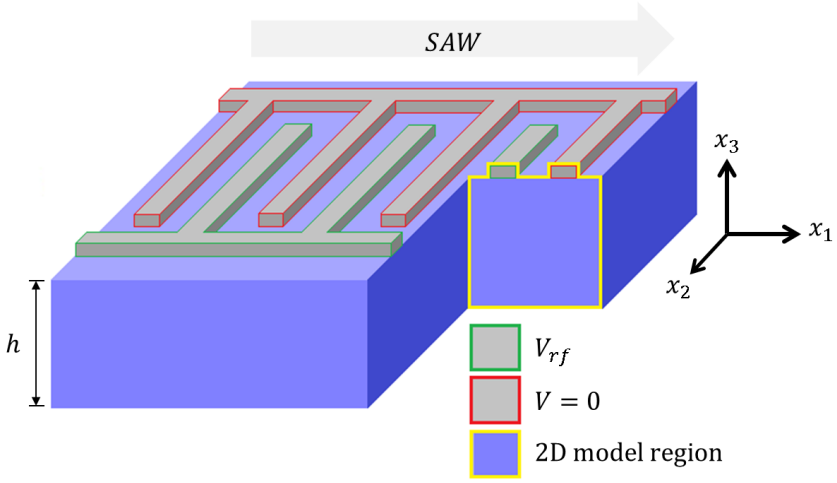

Figure 2.10: highlight of the region of simulation in the bidimensional model (yellow contour). The region can be interpreted as a "unit cell" which is to be repeated indefinitely.

acoustic decay parameter, which is different for each material, and φ_j is a phase factor.

We now present our first simulation model, which intends to study the acoustic and piezoelectric properties of several materials of our interest. These were chosen to be Zinc Oxide (ZnO) and Z-cut Lithium Niobate ($LiNbO_3$), mainly because of their strong piezoelectricity. They are also being studied in laboratory by our experimental group and, thus, the importance of this work. The objective at this stage is to characterize piezoelectric materials and observe Rayleigh modes using our model, verifying the agreement of our results to those presented by the literature.

2.4 The acoustics simulation model

The acoustics model is quite general and should work for any piezoelectric material. It consists of two domains: the aluminium IDT fingers and the piezoelectric substrate.

As the motion of a Rayleigh SAW occurs in the x_1Ox_3 plane (shown in Figure 2.10), a bidimensional model is adequate. This provides great computational advantages, as COMSOL Multiphysics makes use of the finite element method (FEM) [28] and, thus, the number of discrete elements is greatly reduced when compared to a three-dimensional one. Figure 2.10 highlights the region of simulation, which can be regarded as a "unit cell" in the x_1Ox_3 plane. The surface is assumed to be the x_1Ox_2 plane at which $x_3 = 0$.

The simulation geometry is presented in Figure 2.11 along with the boundary conditions. The unit cell is $5.6\mu m$ wide, which is the SAW wavelength for all models in this work. The inset exhibits the materials used, their respective thicknesses and boundary conditions.

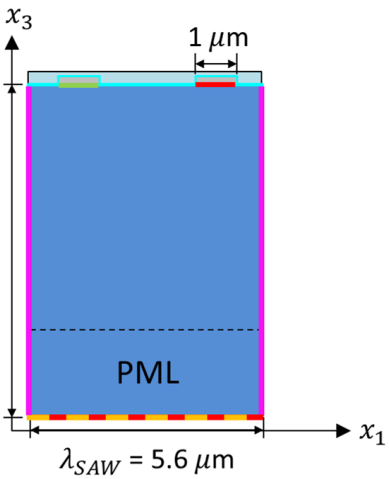

Material	Geometry	Thickness (µm)
Air	Top cover	0.3
Aluminium	IDTs	0.2
ZnO	Substrate	14.0

Boundary Conditions	
Electric Potential	$V = V_{RF}$
Ground	$V = 0$
Fixed Constraint	$\lvert\vec{u}\rvert = 0$
Periodic Condition (*continuity*)	$\phi_L = \phi_R$ $\vec{u}_L = \vec{u}_R$
Free	T = 0

Figure 2.11: representation of the geometry and boundary conditions for the acoustics simulation model. Inset: materials used, layer thicknesses and boundary conditions applied.

Proper boundary conditions are necessary to describe the motion of Rayleigh SAWs. These conditions are imposed to the wave equation 2.36 and solved by COMSOL. In Figure 2.11, the left electrode is at V_{rf} (green). The right electrode and the bottom of the substrate are at $V = 0$ (red). The latter is also constrained, that is, the displacement vector is null ($|\vec{u}|= 0$, in orange). The surface is stress-free 2.37c (cyan). To the sides of the substrate, we impose the periodicity condition, in magenta:

$$\vec{u}_L = \vec{u}_R, \tag{2.41a}$$

$$\phi_L = \phi_R, \tag{2.41b}$$

where ϕ is the piezoelectric potential. The indexes L and R denote the left and right sides, respectively.

The *Perfectly Matched Layer* (PML) [34] is used in this model. It creates an artificial damping for acoustic propagation, imposing an exponential decay of u_1 and u_3 along the x_3 direction. In this way, we are able to obtain the solutions that correspond to Rayleigh SAWs, and filter the bulk components which would otherwise also satisfy equation 2.36.

It must be pointed out that our model does not include acoustic (damping) or electrical (acousto-electrical coupling) losses other than the PML. In this way, our first interest is to be able to predict the acoustic resonances of a system and obtain reasonable values for the physical parameters of interest, like amplitude of particle displacements, strains, and piezoelectric fields. A quantitative analysis could, however, be easily performed by fitting experimental results using our model.

2.4.1 Determination and characterization of SAW modes

The search for acoustic resonances can be done in two ways. If the frequency region of the resonance is known, the mode can be found by solving the eigenvalue problem. On the other hand, if the frequency region is unknown (which is usually the case of more complicated layered systems) a frequency scan (sweep) can be performed in order to find the resonances.

The eigenvalue solver (or eigenfrequency solver, in this case) finds the solution to linear or linearized eigenvalue problems, also called "eigenfrequency problems". The FEM discretization leads to the generalized eigenvalue system:

$$\begin{cases} (\lambda - \lambda_0)^2 M\Psi - (\lambda - \lambda_0) N\Psi + O\Psi + P\Lambda = 0, \\ Q\Psi = 0, \end{cases} \tag{2.42}$$

where λ is the eigenvalue, λ_0 is the linearization point (taken to be zero in our models). The solver evaluates M, N, O, P and Q for the solution vector Ψ. If $M = 0$, equation 2.42 is a linear eigenvalue problem; otherwise, it is a quadratic eigenvalue problem. To solve the latter case, COMSOL reformulates it as a linear eigenvalue problem.

At this stage, this method is being used to solve equation 2.36; the eigenvalues corresponding to the displacements (u_i) and the piezoelectric potential (ϕ). The output solutions of this section are then normalized to the corresponding values of a maximum piezoelectric potential amplitude of $max(|\phi|) = 1$V.

Figures 2.12(a) and 2.12(b) show the results for the sweeps performed in order to obtain the lowest SAW modes in ZnO and $LiNbO_3$, respectively. The plots show the maximum value achieved by the piezoelectric potential, in arbitrary units, with respect to the acoustic frequency for ranges of about 200 MHz. This is a good parameter for obtaining SAW modes in a frequency sweep, because the energy density for such modes is concentrated in the near-surface region, which usually leads to higher piezoelectric potential amplitudes. The acoustic energy density, for instance, would also be adequate in this task. Bulk modes, on the other hand, typically present lower acoustic energy densities when compared to SAW modes, because they are spread over larger portions of the substrate.

Figure 2.12 also presents the effects of a PML in the search for SAW modes via frequency sweeps. The red curves represent sweeps performed without it. In those cases, other modes were detected, which afterwards were confirmed to be bulk modes. Inclusion of the PML (blue-dotted scans) allows only SAW modes to be present in the sweeps. The peaks obtained for both materials at $f_{SAW} = 481.1$ MHz for ZnO and $f_{SAW} = 686.0$ MHz for $LiNbO_3$ were indeed verified to be Rayleigh SAW modes, as shown in the sequence.

The SAW propagation velocities can be obtained from the resonance frequencies through

the relation

$$v_{SAW} = \lambda_{SAW} f_{SAW}, \tag{2.43}$$

which provides the velocities $v_{SAW} = 2694\ m.s^{-1}$ for ZnO and $v_{SAW} = 3843\ m.s^{-1}$ for Z-cut $LiNbO_3$. These values agree very well with others reported in literature. References [35, 36] report velocities of about $v_{SAW} = 2700\ m.s^{-1}$ and $v_{SAW} = 3900\ m.s^{-1}$ for ZnO and $LiNbO_3$, respectively. The small discrepancies are attributed to differences between the material constants used in our calculations and those of the references.

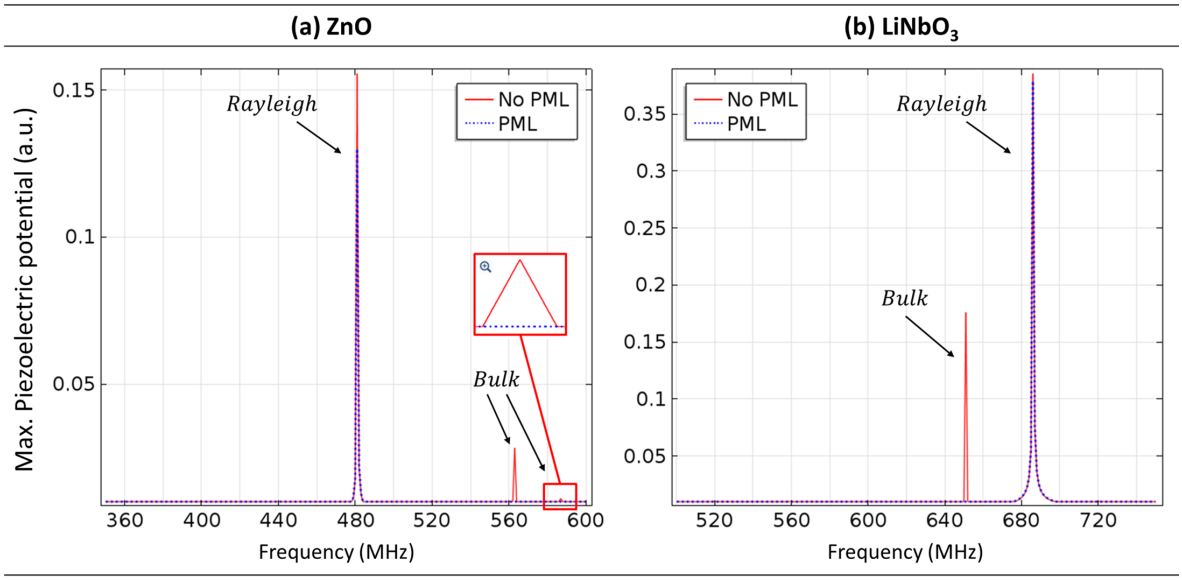

Figure 2.12: frequency sweep for maximum piezoelectric potential in (a) ZnO (c-axis) and (b) Z-cut $LiNbO_3$. The red plots indicate sweeps performed without the PML, while the blue-dotted plots were obtained by including the PML. The resonant modes present exclusively in the red plots were verified to be bulk modes.

Figure 2.13 exhibits the piezoelectric potential, total displacement ($|\vec{u}|$) and displacement components obtained for ZnO and $LiNbO_3$ via eigenfrequency solver. It depicts Rayleigh SAW modes, as the particle displacement is confined to the surface; there's no out-of-plane movement, and u_1 and u_3 are out of phase by $\pi/2$. This produces an elliptical movement whose eccentricity increases with the depth of the substrate. The piezoelectric potentials from Figure 2.13 can affect the electronic and spin properties of nanostructured systems, such as quantum wells and nanowires, as demonstrated experimentally [7, 8, 9].

During carrier acoustic transport, the piezoelectric field component parallel to x_3 is responsible for electronic band modulation, while the one along the x_1 axis is related to transport (carrier, spin) phenomena. These components are also responsible for the electro-optic effect, which will be addressed in chapter 4. Our model has obtained values of E_1 and E_3, exhibited in Figure 2.14, which lie in the same order of magnitude as those reported for ZnO [9]. Figure

2.14 also exhibits the strains associated to the eigenfrequency study. Typical values for these can be found in the literature between $10^{-3} - 10^{-4}$, which lies in the same order of magnitude as the ones encountered in our model.

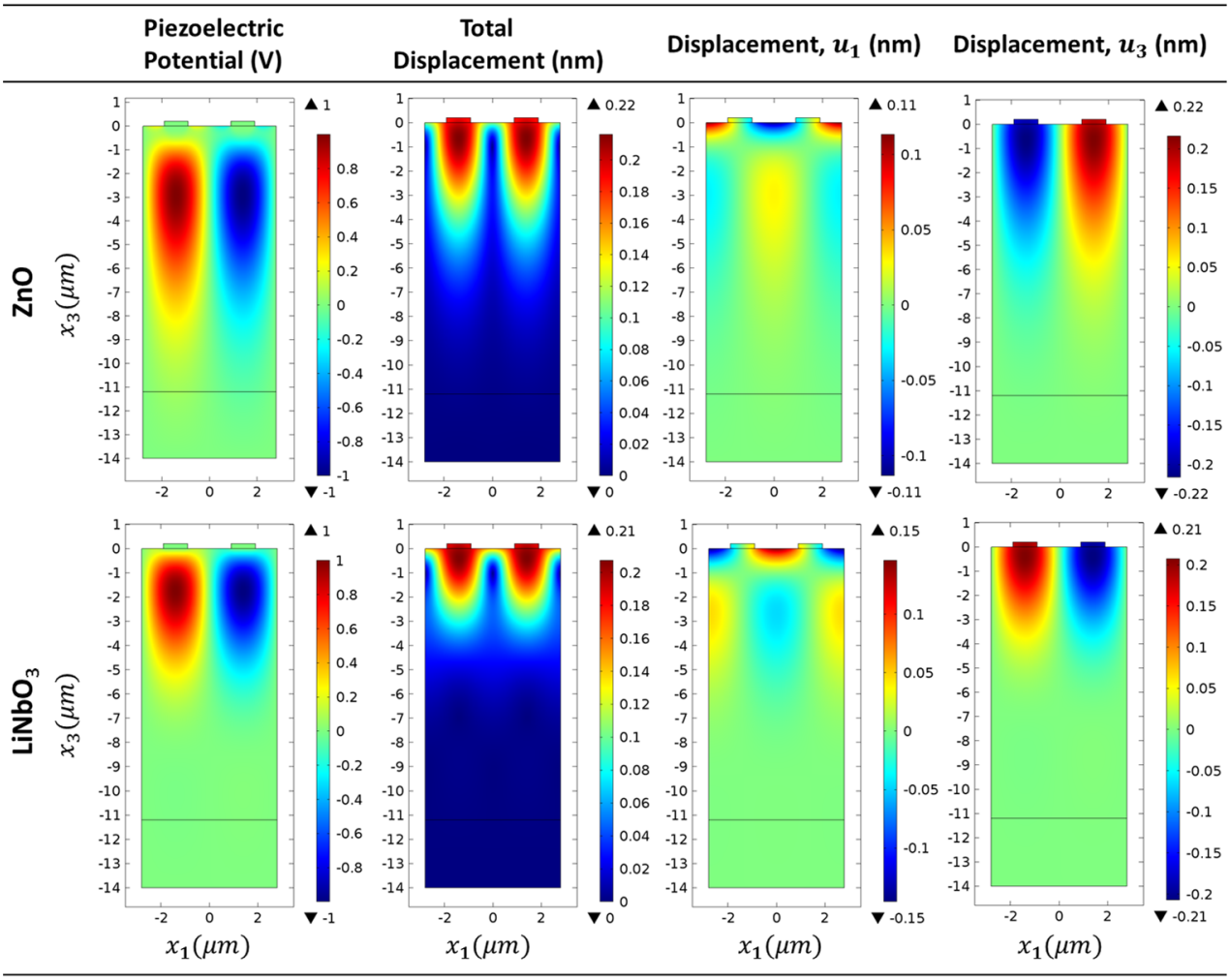

Figure 2.13: piezoelectric potential, total displacement, displacement components for ZnO and $LiNbO_3$ at the eigenfrequencies $f_{SAW} = 481.13$ MHz and $f_{SAW} = 686.17$ MHz, respectively.

2D color graphs can give an overall idea of the fields distribution inside the geometry, but we are also interested in observing the decay profiles of those fields. This is presented in Figure 2.15, where we have performed cut lines below the center of either IDTs, from the surface to the bottom of the substrate.

The displacement and piezoelectric potential profiles shown in Figure 2.15 agree with equations 2.24(a-b), as they exhibit exponential decays. It is observable that ZnO substrates are more susceptible to acoustic penetration when compared to Z-cut $LiNbO_3$. The strain profiles presented in Figure 2.15, however, give evidence that the latter possesses higher acoustic energy density in the near-surface region.

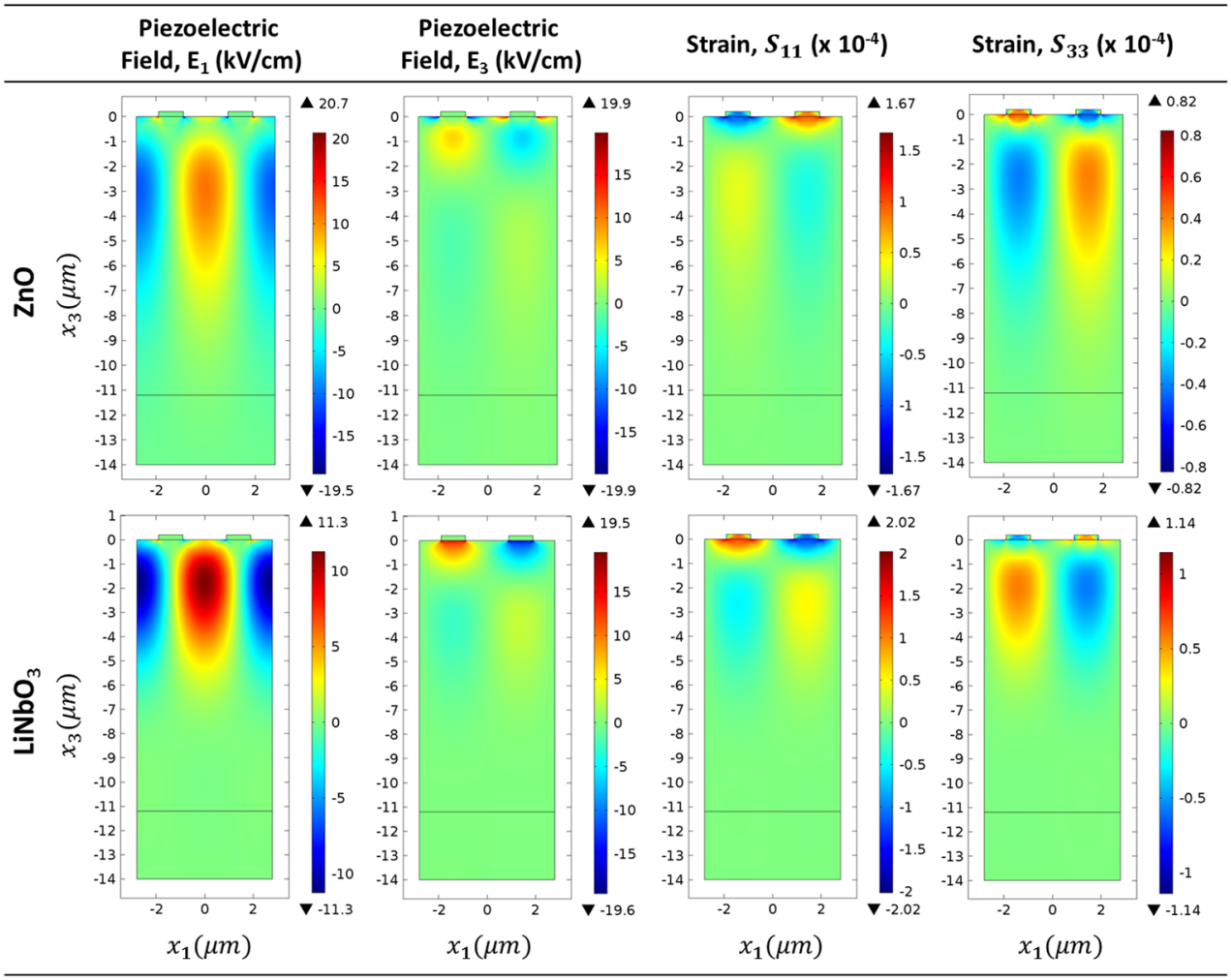

Figure 2.14: piezoelectric field and strain components in ZnO and $LiNbO_3$ at the eigenfrequencies $f_{SAW} = 481.13$ MHz and $f_{SAW} = 686.17$ MHz, respectively.

These profiles are very important for the characterization of piezoelectric structures. They suggest that one could predict the optimized distance from the surface to insert nanostructures or, in our case, optical cavities. Depending on the interest, such distances could mean, for example, the region where strain is maximized (which is usually the case).

It has become evident that the piezoelectric effect is more intense in regions near the surface, but not at the surface. That is because piezoelectricity requires many atoms to become macroscopically relevant. Atoms of the surface layer, for example, have half as atomic bonds as the inner atoms have. The second layer sees exactly half but one less layers than the first. The third layer sees half but one less layers than the second, and so on. Therefore, the deeper an atom is in the substrate, the more neighbours, second neighbours, etc. it has. On the other hand, an atom located too far from the surface would acquire less acoustic energy. Thus, the piezoelectric effect must be stronger in a mid-term depth. Of course, the strain on the surface

is very strong. That is due to the vibrations of the IDTs, which can be confirmed by glancing at the displacement profiles, and remembering the definition of strain from equation 2.12.

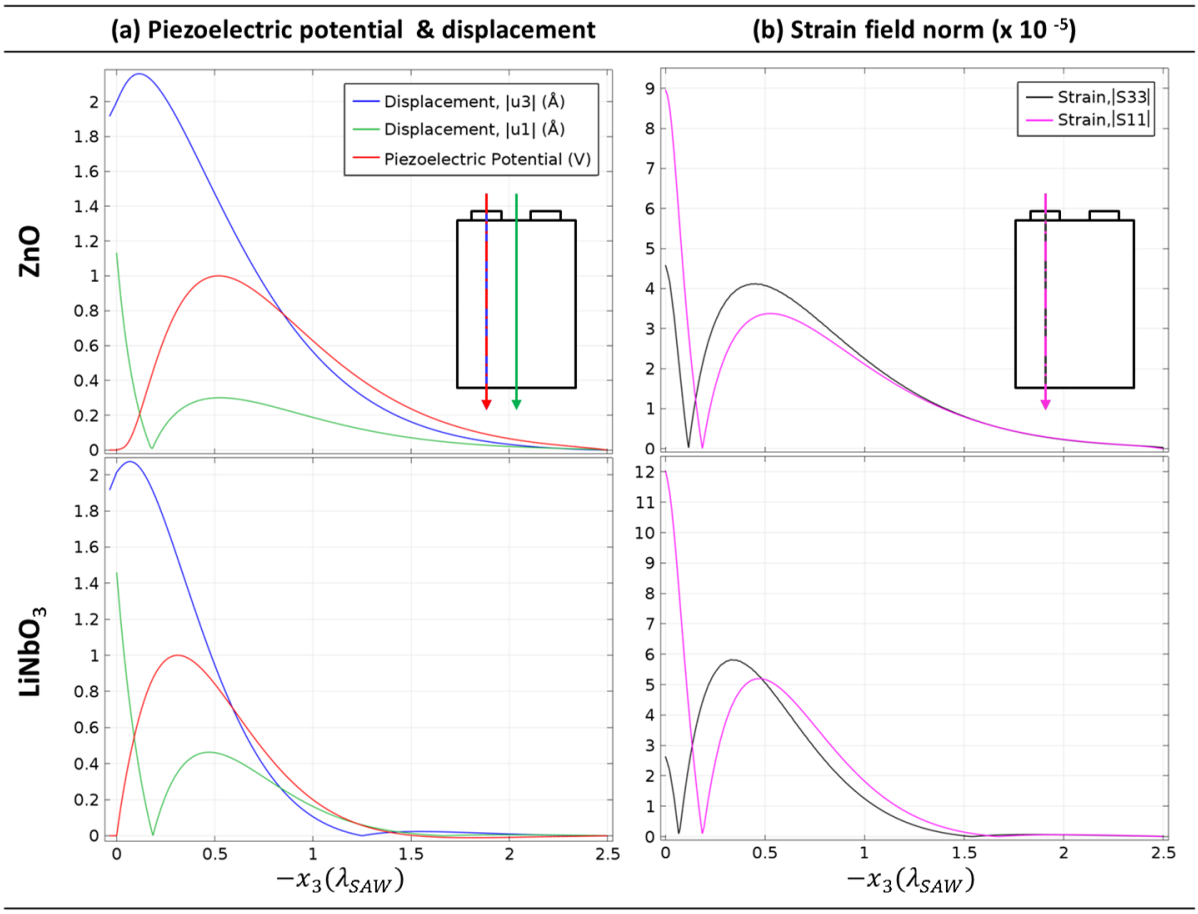

Figure 2.15: profiles for (a) piezoelectric potential and displacement components, and (b) strain norms in both ZnO and $LiNbO_3$. Insets: the transverse cut-lines performed to obtain these profiles.

We conclude this chapter by arguing that we're able to predict and calculate the acoustic and piezoelectric properties of SAWs in any piezoelectric material. We have used ZnO and Z-cut $LiNbO_3$ single substrates to validate our model, and showed that our results can be fairly compared to the literature. In the following chapter, we'll be describing the optical properties of layered systems, i.e., planar optical microcavities (POMCs), and in chapter 4 we address the influence of SAW propagation on the optical response of POMCs designed with piezoelectric material layers.

Chapter 3

The planar optical microcavity

3.1 Introduction

This chapter introduces the optical system on which we intend to observe the acousto-optic modulation - namely, the planar optical microcavity (POMC). Our approach makes use of classical wave theory, building this device from the starting point of a single dielectric layer. Later, we present the *BMs*, which are being addressed via the Transfer Matrix (TM) method. After that, we introduce the POMC itself. The last section is dedicated to the simulation model for such a device, which makes use of concepts presented in this chapter to optimize the design of POMCs.

3.2 The Fabry-Perot cavity

We begin by addressing what happens when light interacts with a single dielectric layer. Figure 3.1 exhibits a very thin dielectric slab with width d (or, similarly, a pair of facing mirrors separated by a tiny distance), known as the *Fabry-Perot cavity* [17]. It possesses refractive index n, being surrounded by air. Assuming there is no absorption, when a light beam with electric field E_0 incides on the left air/cavity interface, part of its intensity is reflected ($E_0 r$) and the other part is transmitted ($E_0 t$). The transmitted beam undergoes the same procedure when it reaches the next interface, and sucessive reflections and transmissions occur. Therefore, the reflected and transmitted beam intensities are the summation of all orders on the left (orange arrows) and right (red arrows) sides of Figure 3.1, respectively.

The optical path difference between two sucessive transmitted beams, represented by the black bold arrows, is:

$$\Delta d = 2d \cos\theta, \tag{3.1}$$

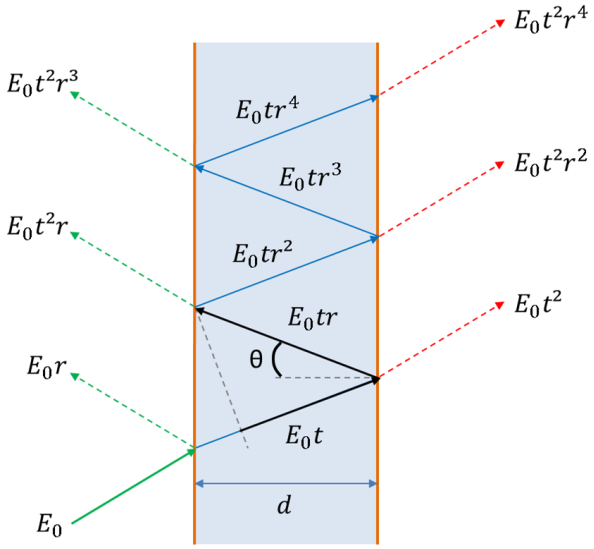

Figure 3.1: representation of a Fabry-Perot cavity. It consists of a thin dielectric slab. The incident light beam on the left air/cavity interface undergoes a sucession of transmissions and reflections. The total transmitted and reflected intensities are represented by the red and green arrows, respectively. The black bold arrows represent the optical path difference between two consecutive beams.

which implies in a phase difference, δ, of

$$\delta = 2kd\cos\theta = \frac{4\pi}{\lambda}d\cos\theta, \tag{3.2}$$

where k and λ are the wave vector and wavelength of light in the dielectric medium, respectively. In terms of k_0, the wave vector in free-space, δ becomes

$$\delta = 2k_0nd\cos\theta, \tag{3.3}$$

where the product nd is known as the *optical thickness*, i.e., the distance light "sees" when inside the dielectric medium. The transmitted beams will produce an interference pattern where the total light intensity is a geometric series with ratio $r^2e^{i\delta}$:

$$E_T = E_0t^2 + E_0t^2r^2e^{i\delta} + E_0t^2r^4e^{i\delta} + \ldots = \frac{E_0t^2}{1 - r^2e^{i\delta}}. \tag{3.4}$$

where the quantities r and t are the reflection and transmission coeficients, respectively. Accounting for the phase associated to reflections, δ_r, we can write $r = |r|e^{i\delta_r/2}$. Thus, equation 3.4 becomes

$$E_T = \frac{E_0t^2}{1 - |r|^2e^{i\Delta}}, \tag{3.5}$$

where $\Delta = \delta + \delta_r$ is the total phase difference between two consecutive transmitted beams.

Multiplying equation 3.5 by its complex conjugate gives

$$I_T = I_0 \frac{T^2}{|1 - R^2 e^{i\Delta}|^2}, \tag{3.6}$$

where we define

$$I_0 = |E_0|^2,\ I_R = |E_R|^2 \text{ and } I_T = |E_T|^2 \tag{3.7a}$$

as the intensities of the incident, reflected and transmitted light beams, respectively, and

$$T = \left|\frac{E_T}{E_0}\right| = |t|^2 \text{ as the } \textit{transmitance}, \tag{3.7b}$$

$$R = \left|\frac{E_R}{E_0}\right| = |r|^2 \text{ as the } \textit{reflectance}, \tag{3.7c}$$

while energy conservation imposes (assuming no absorption occurs)

$$R + T = 1. \tag{3.7d}$$

Equation 3.6 can be rewritten as

$$I_T = I_0 \frac{T^2}{(1 - R^2)} \left[\frac{1}{1 + \mathcal{F} \sin^2\left(\frac{\Delta}{2}\right)}\right], \tag{3.8}$$

where we identify the following:

$$A(\Delta) = \frac{1}{1 + \mathcal{F} \sin^2\left(\frac{\Delta}{2}\right)} \text{ as the } \textit{Airy function} \tag{3.9a}$$

$$\mathcal{F} = \frac{4R}{(1 - R)^2} \text{ as the } \textit{Finesse}. \tag{3.9b}$$

The Airy function (Figure 3.2) is responsible for the interference pattern, while Finesse is defined as the free spectral range divided by the (full width at half-maximum) bandwidth of its resonances. When $\mathcal{F}$ increases, so does the sharpness of the optical resonances. The behaviour of equation 3.8 is such that, for an integer $N = 1, 2, 3...$,

$$\Delta = 2N\pi \text{ implies that the transmitted intensity is } \textbf{maximum}. \tag{3.10a}$$

$$\Delta = (2N + 1)\pi \text{ implies that the transmitted intensity is } \textbf{minimum}. \tag{3.10b}$$

The integer N is known as the *order of interference*.

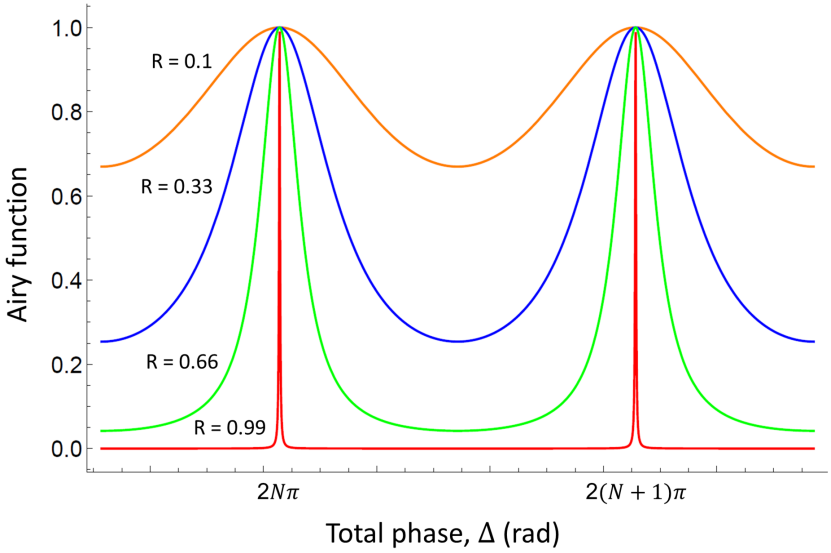

Figure 3.2: plot of the Airy function, which describes the interference pattern for a Fabry-Perot cavity. Several reflectance values are presented. As these values increase, so does the finesse (equation 3.9b), and the peaks become more sharp.

Therefore, we conclude that a single dielectric layer can behave either as a transmissive, or as a reflective medium, depending on its construction. Of course, equation 3.10b alone is not sufficient condition to obtain a mirror. We now dedicate our attention to mirrors to show how these can be constructed.

3.3 The Bragg Mirror

The minimum transmistance, or, equivalently, the maximum reflectance, is achieved when a dielectric layer satisfies equation 3.10b. The phase associated to a maximum reflection is $\delta_r = \pi$, which allows us to write

$$2k_0 nd\cos\theta + \pi = (2N+1)\pi. \tag{3.11}$$

In this way, equation 3.11 gives, for the first order of interference,

$$k_0 nd\cos\theta = \frac{\pi}{2}. \tag{3.12}$$

Considering normal light incidence and TE-polarization, the reflectance (R) is then given by [17, pg. 44]

$$R = \left|\frac{n-1}{n+1}\right|^2. \tag{3.13}$$

Figure 3.3 shows the behaviour of this equation. It can be observed that the regime where

a single layer would behave as a mirror can only be achieved at exorbitant values of n. Thus, equation 3.12 is a requirement, but not a sufficient condition for obtaining a mirror.

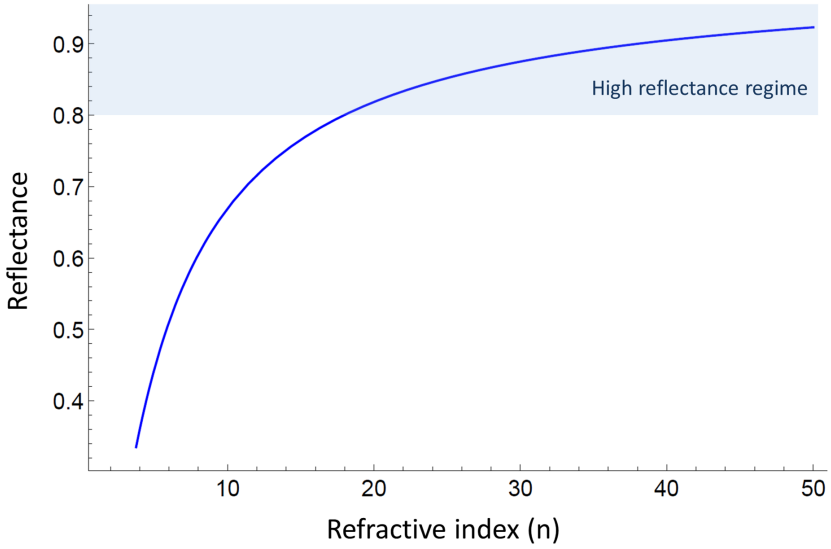

Figure 3.3: plot of equation 3.13. The regime which characterizes a mirror ($R > 0.9$) is unreachable for a single layer due to the exorbitant values of n required.

The concept of a Bragg mirror (BM) involves two different material layers. We name the products $n_H d_H$ and $n_L d_L$ as the high and low optical thicknesses, respectively. Figure 3.4 shows the first three reflected light beams in such a configuration. The green bold arrows indicate the path difference between the 1^{st} and 2^{nd} beams, while the red bold arrows indicate the same for the 2^{nd} and 3^{rd} beams.

In order to obtain maximum reflectance, the reflected beams must match in phase, that is

$$2k_0 n_L d_L = \pi, \tag{3.14a}$$

$$2k_0 n_H d_H = \pi. \tag{3.14b}$$

The phase difference between the 1^{st} and the 3^{rd} beam is

$$2k_0(n_L d_L + n_H d_H) = 2\pi. \tag{3.14c}$$

Thus, equations 3.14(a-c) provide, respectively,

$$n_L d_L = \frac{\lambda_0}{4}, \tag{3.15a}$$

$$n_H d_H = \frac{\lambda_0}{4}, \tag{3.15b}$$

$$(n_L d_L + n_H d_H) = \frac{\lambda_0}{2}. \tag{3.15c}$$

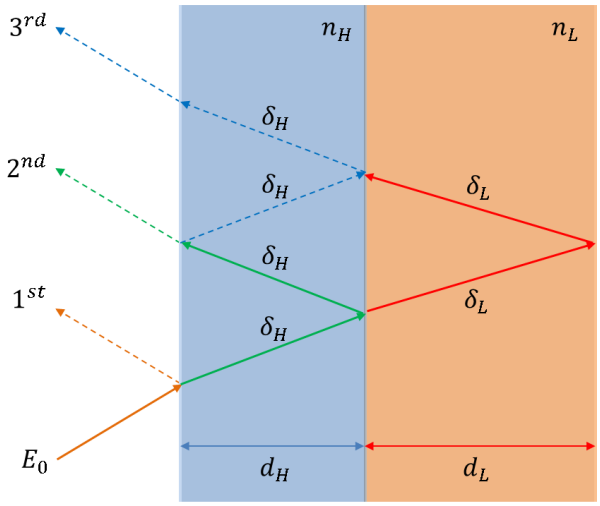

Figure 3.4: three consecutive reflected light beams in a BM. The phase gained when light propagates through each layer is shown, and the arrows indicate the path of each beam.

3.3.1 The transfer matrix method

Equations 3.15(a-c) give the condition for maximum reflectance in a BM, but no information on its value. In order to obtain the reflectance, we use the transfer matrix method [18]. Figure 3.5 exhibits a TE-polarized electric field inside the BM for a light beam which is incident normally from the left. The layers are labeled with the indexes $(s-1)$, s and $(s+1)$, while the forward (green) and backscattered (red) fields have upper indexes $+$ and $-$, respectively.

As the light beam crosses the s^{th} layer, it gains a phase equal to $k_0 n_s d_s$. At any interface, we have that the electric field must be continuous:

$$E_{s-1}^{+} + E_{s-1}^{-} = E_s^{+} e^{ik_0 n_s d_s} + E_s^{-} e^{-ik_0 n_s d_s}, \tag{3.16}$$

and also the magnetic field:

$$H_{s-1}^{+} + H_{s-1}^{-} = H_s^{+} e^{ik_0 n_s d_s} + H_s^{-} e^{-ik_0 n_s d_s}, \tag{3.17}$$

where the following relation between electric and magnetic fields holds: $E_s^{\pm}/\eta_s = \pm H_s^{\pm}$, with η_s being the speed of light in the s^{th} layer. By defining the total electric and magnetic fields at each layer as

$$E_s = E_s^{+} + E_s^{-}, \tag{3.18a}$$

$$H_s = H_s^{+} + H_s^{-}, \tag{3.18b}$$

we obtain the following linear system:

$$\begin{bmatrix} E_{s-1} \\ H_{s-1} \end{bmatrix} = \begin{bmatrix} \cos(k_0 n_s d_s) & (i/\eta_s)\sin(k_0 n_s d_s) \\ i\eta_s \sin(k_0 n_s d_s) & \cos(k_0 n_s d_s) \end{bmatrix} \begin{bmatrix} E_s \\ H_s \end{bmatrix}. \tag{3.19}$$

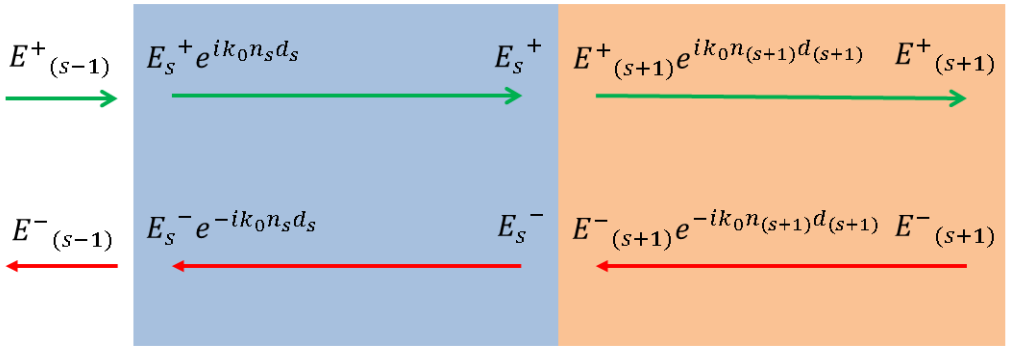

Figure 3.5: electric field associated to a TE-polarized light beam that is incident normally to a BM from the right. The incident and backscattered fields are represented by their analytic expressions above the green and red arrows, respectively.

Equation 3.19 relates the fields from the $(s-1)^{th}$ layer to the s^{th} layer. Two layers must be considered when dealing with the BM, which gives

$$\begin{bmatrix} E_0 \\ H_0 \end{bmatrix} = \begin{bmatrix} \cos(\xi) & (i/\eta_H)\sin(\xi) \\ (i\eta_H)\sin(\xi) & \cos(\xi) \end{bmatrix} \begin{bmatrix} \cos(\chi) & (i/\eta_L)\sin(\chi) \\ (i\eta_L)\sin(\chi) & \cos(\chi) \end{bmatrix} \begin{bmatrix} E_s \\ H_s \end{bmatrix}, \tag{3.20}$$

where $\xi = k_0 n_H d_H$, $\chi = k_0 n_L d_L$, E_0 and H_0 are the electric and magnetic fields in air, respectively. Applying conditions 3.14(a-b), this reduces to

$$\begin{bmatrix} E_0 \\ H_0 \end{bmatrix} = \begin{bmatrix} -\frac{\eta_L}{\eta_H} & 0 \\ 0 & -\frac{\eta_H}{\eta_L} \end{bmatrix} \begin{bmatrix} E_s \\ H_s \end{bmatrix}. \tag{3.21}$$

Thus, for q pairs of layers and $\eta_s = c/n_s$, with c being the speed of light in vacuum,

$$\begin{bmatrix} E_0 \\ H_0 \end{bmatrix} = \begin{bmatrix} -\frac{n_H}{n_L} & 0 \\ 0 & -\frac{n_L}{n_H} \end{bmatrix}^q \begin{bmatrix} E_s \\ H_s \end{bmatrix}. \tag{3.22}$$

The power transmitted and reflected can be obtained by using the following relations [18]:

$$E_0 = 1 - r, \tag{3.23a}$$

$$H_0 = 1 + r, \tag{3.23b}$$

$$E_s = H_s = t. \tag{3.23c}$$

The reflectance is thus given by

$$R = \left[\frac{(-\frac{n_L}{n_H})^q - (-\frac{n_H}{n_L})^q}{(-\frac{n_L}{n_H})^q + (-\frac{n_H}{n_L})^q}\right]^2. \tag{3.24}$$

Equation 3.24 gives evidence of the dependence of the reflectance on both the refractive index contrast and q (number of pairs of BMs). In contrast with equation 3.13 for a single layer, achieving reflectance values close to unity is feasible. Figure 3.6 exhibits the behaviour of equation 3.24. It can be seen that, even for low refractive index contrasts, the reflectance can reach values very close to unity when the number of pairs is increased.

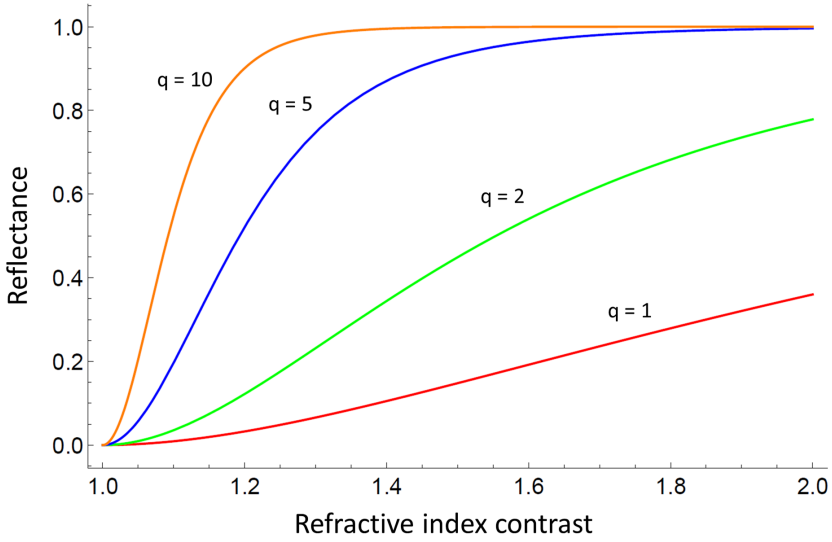

Figure 3.6: plot of equation 3.24 as function of the refractive index contrast and number of BMs, q.

3.4 The photonic band gap

Multistacks of BMs are also known as *Distributed Bragg Reflectors* (DBRs). Their reflectance values are up to unity, with the disadvantage of possessing a limited spectral width. If we do not impose conditions 3.14(a-b) to equation 3.20, the latter becomes dependent on sines and cossines of $k_0 n_L d_L$ and $k_0 n_H d_H$, producing a reflectance spectrum. As an example, Figure 3.7 depicts the reflectance spectrum constructed via TM method for a DBR with $q = 5$

pairs of quarter-wavelength ($n_H d_H = n_L d_L = \lambda_0/4$) layers, where $n_H = 3.7$ and $n_L = 1.5$. It is characterized by the presence of a large band width where the reflectance is maximum, known as the *Photonic Band Gap* (PBG), since no photonic mode is allowed within this energy range.

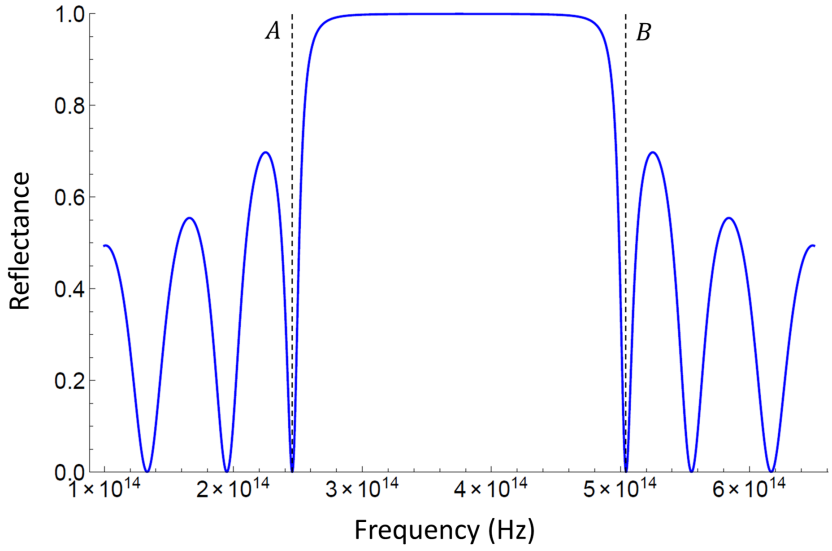

Figure 3.7: analytical reflectance spectrum under normal light incidence. The DBR possesses $q = 5$ pairs of quarter-wavelength layers with $n_H = 3.7$ and $n_L = 1.5$.

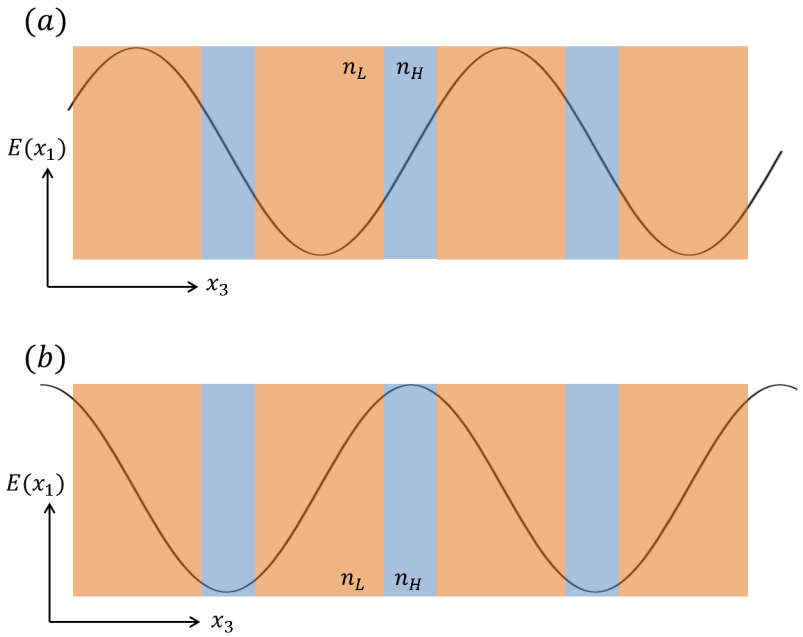

Figure 3.8: positioning of the electric field inside the DBR. Exclusively in this example, the light beam is polarized along x_1 and its wave vector points towards x_3. In (a), the field's crests and valleys are contained within the low refractive index layers. In (b), these are contained within the high refractive index layers.

It appears due to the positioning of the electric field inside the periodic array of layers, with periodicity given by a:

$$2a = 2(n_L d_L + n_H d_H) = \lambda_0. \tag{3.25}$$

The electric field can be positioned in many ways inside the structure of the DBR as long as it satisfies equation 3.25. Figure 3.8 illustrates the two extreme cases. In Figure 3.8a, the energy of the electric field is more contained within the low refractive index layers, which corresponds to lower wavelengths, or to higher frequencies (point B in Figure 3.7). The opposite is happening in Figure 3.8b, corresponding to lower frequencies (point A in Figure 3.7).

Between points A and B, the electric field can assume any intermediary position. The maximum value of $\Delta f = f(B) - f(A)$ occurs when equations 3.15a and 3.15b hold.

3.5 The planar optical microcavity

The structure of a POMC is achieved by inserting a layer that behaves as a photonic defect - namely, the optical cavity - between two BMs, as in Figure 3.9. In favor of maintaining the periodicity of the structure constant, condition 3.26 holds:

$$n_c d_c = \frac{\lambda_0}{2}, \tag{3.26}$$

where n_c and d_c are the refractive index and thickness of the cavity, respectively.

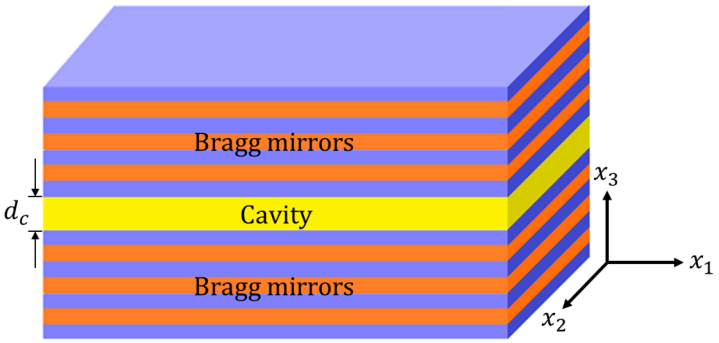

Figure 3.9: illustration of a POMC. The cavity layer, represented in yellow, is inserted between two BMs.

The POMC can also be referred to as a unidimensional photonic crystal, as its periodicity lies in only one direction (in this case, the x_3 direction). It can effectively confine light inside the cavity, which can be observed in the reflectance spectrum for such a device. As an example, Figure 3.10 exhibits the reflectance spectrum, constructed via TM method, for a 800 nm cavity inserted between two BMs ($q = 5$, $n_H = 3.7$ and $n_L = 1.5$). It becomes evident the appearance

of a deep valley right in the middle of the PBG, which corresponds to the frequency $f_0 = 374.74$ THz (or $\lambda_0 = 800$ nm).

Once inside the cavity, the light beam becomes trapped between two extremely reflective mirrors, suffering multiple reflections before it can finally escape. This is referred to as a light-matter coupling. But one could also think in terms of photons with energy $E_0 = \hbar\omega_0 = 1.5498$ eV that would otherwise pass through the cavity in about $10^{-16}s$, but happen to do it in much longer times. The lifetime of photons in the cavity is related to the *Quality Factor*, Q, according to equation 3.27 [37]:

$$Q = 2\pi f_0 \tau_c, \tag{3.27}$$

where $\tau_c = n_c d_c / c(1 - R)$ is the photon lifetime inside the cavity and R is the maximum reflectance of the PBG [37].

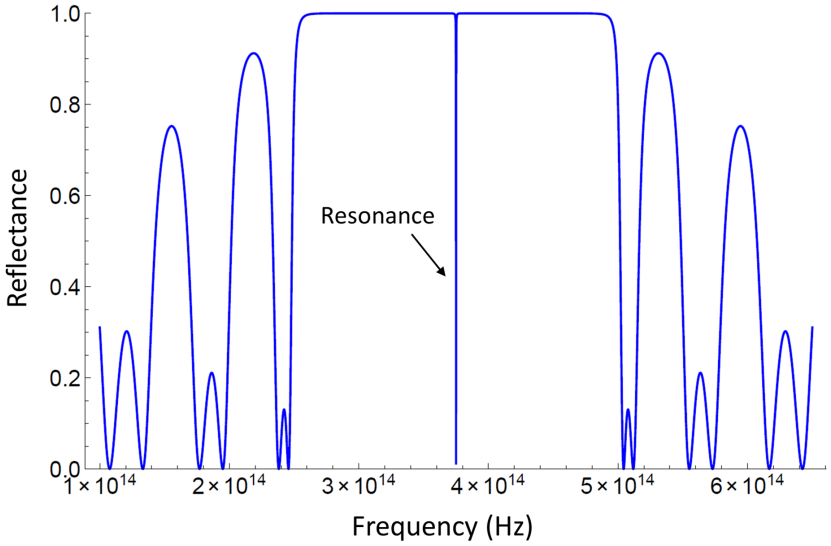

Figure 3.10: reflectance spectrum for a POMC with $q = 5$ BMs with $n_H = 3.7$ and $n_L = 1.5$, and a 800 nm cavity. The PBG presents a deep valley at $f_0 = 374.74$ THz.

The Q-factor can be estimated from full width at half maximum (FWHM) of the reflectance dip as

$$Q = \frac{f_0}{\Delta f} = \frac{\omega_0}{\Delta\omega} = \frac{\lambda_0}{\Delta\lambda}. \tag{3.28}$$

As an example, the estimated Q-factor for the structure from Figure 3.10 is $Q = 3747$. According to equation 3.27, this would give an average lifetime of $\tau_c = 1.6 \times 10^{-12}$ s for photons inside the cavity. Two (micropillars and 2D photonic crystals) and even three-dimensional (microspheres) optical cavities are currently being studied by the scientific community. These can offer even higher Q-factors, as light becomes confined in more degrees of freedom [13].

3.6 The optics simulation model

We now present our simulation model developed in COMSOL Multiphysics for a POMC, where we're using the concepts developed during this chapter. It must be consistent with the model presented in chapter 2, for it is the planar device over which the IDTs will be generating SAWs. Therefore, our work with ZnO and $LiNbO_3$ continues. We also make use of SiO_2, as (i) this material can be grown through oxygen assisted sputtering processes, which is a technology accessible to our experimental team; (ii) ZnO and $LiNbO_3$ are strong piezoelectric materials, and BMs composed of such materials should strengthen the strain field in the active region of the cavity due to larger penetration of SAW-induced strain fields; (iii) they present a good refractive index contrast with SiO_2; (iv) ZnO/SiO_2 devices have already been fabricated and studied [38], allowing us to test the results of our model.

The 2D unit cell is in the x_1Ox_3 plane and its width is the SAW wavelength, 5.6 μm. The cavity is designed for $\lambda_0 = 800$nm, and equations 3.15(a-c) and 3.26 hold for the BMs and the optical cavity. The geometry and boundary conditions are presented in Figure 3.11, where the SiO_2 cavity is inserted between q pairs of BMs composed of either ZnO/SiO_2 or $LiNbO_3/SiO_2$. The inset summarizes material compositions, geometric entities and boundary conditions.

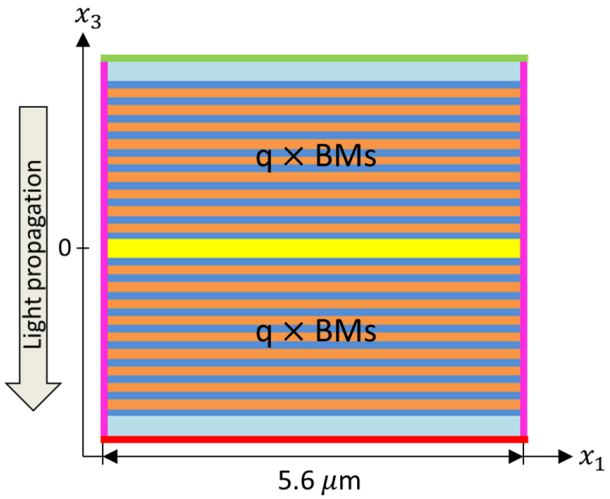

Material	Geometry	Ref. Index	Thickness (nm)
Air	Top/bottom cover	1.0	300
ZnO	High ref. index layer	1.974	101.32
$LiNbO_3$		2.175	91.95
SiO_2	Low ref. index layer	1.453	137.65
SiO_2	Cavity	1.453	275.29

Boundary Conditions	
Port 1	Light excitation, measure of R
Port 2	Light absorption, measure of T
Continuity	Floquet periodicity

Figure 3.11: geometry and boundary conditions for the simulation model of a POMC. Inset: material composition, geometric entities, refractive indexes, layer thicknesses and boundary conditions.

The boundary conditions are as follows: the Port 1 (green) and Port 2 (red) conditions (Figure 3.11) are responsible for light excitation at arbitrary incidence angles, θ, and also for measuring the reflected intensity (s_{11} parameter). The latter absorbs light and measures

the transmitted intensity (s_{21} parameter). The s-parameters (or scattering parameters) are elements of the scattering matrix, which describes the electrical behaviour of linear electrical networks. In 2-port networks, the relationship between the reflected/incident power waves and the s-parameters is given by:

$$\begin{bmatrix} E_1^- \\ E_2^- \end{bmatrix} = \begin{bmatrix} s_{11} & s_{12} \\ s_{21} & s_{22} \end{bmatrix} \begin{bmatrix} E_1^+ \\ E_2^+ \end{bmatrix}, \tag{3.29}$$

where E_1^+ and E_1^- are the incident and reflected waves on Port 1, respectively, while E_2^+ and E_2^- are the incident and reflected waves on Port 2, respectively. By using the Port boundary conditions, we are able not just to excite light with selected incident angles, but also to obtain the reflectance spectrum, defined by $R = |s_{11}|^2$. The Floquet periodicity, imposed to the side walls of the unit cell (Figure 3.11, in magenta), states that the electric field on one side of the unit cell equals to the solution on the other side multiplied by a complex-valued phase factor. The phase shift is evaluated from the x_3 component of the wave vector. In other words, it makes sure that the electromagnetic field behaves as Bloch waves inside the geometry, with periodicity given by equation 3.25. This is to be consistent with the reasoning behind the appearance of the PBG from section 3.4.

The simulation procedure makes use of both frequency sweeps and eigenvalue solvers, just as in section 2.4.1. The former must be performed to obtain the reflectance spectrum for each different geometry/material combination and angle of incidence. The latter provides a quick and easy access to the resonance modes, so we can observe the electric field distribution inside the geometry. This time the eigenvalue solver applies to the wave equation for electromagnetic waves in dielectric materials, that is, Maxwell's equations:

$$\frac{\partial^2 \vec{E}}{\partial^2 t} = \frac{1}{\eta_s^2}(\vec{\nabla}.\vec{E}), \tag{3.30a}$$

$$\frac{\partial^2 \vec{H}}{\partial^2 t} = \frac{1}{\eta_s^2}(\vec{\nabla}.\vec{H}), \tag{3.30b}$$

where $\vec{E}$ and $\vec{H}$ are the electric and magnetic fields, and η_s is the speed of light inside the s^{th} layer. The eigenvalues in this case are the electric field vector components, where we have chosen the eigenvalues to be normalized to the maximum electric field in the structure which, for the POMC, is the electric field in the optical cavity layer. Thus, in our results, the electric field is being presented in arbitrary units (a.u.) and ranges from 0 to 1.

3.6.1 Determination of optical resonances and Q-factors in POMCs

We begin by performing a frequency sweep around the expected resonance frequency in order to obtain the spectral reflectance curves. At this stage, the results obtained via COMSOL were compared to transfer matrix (TM) method calculations.

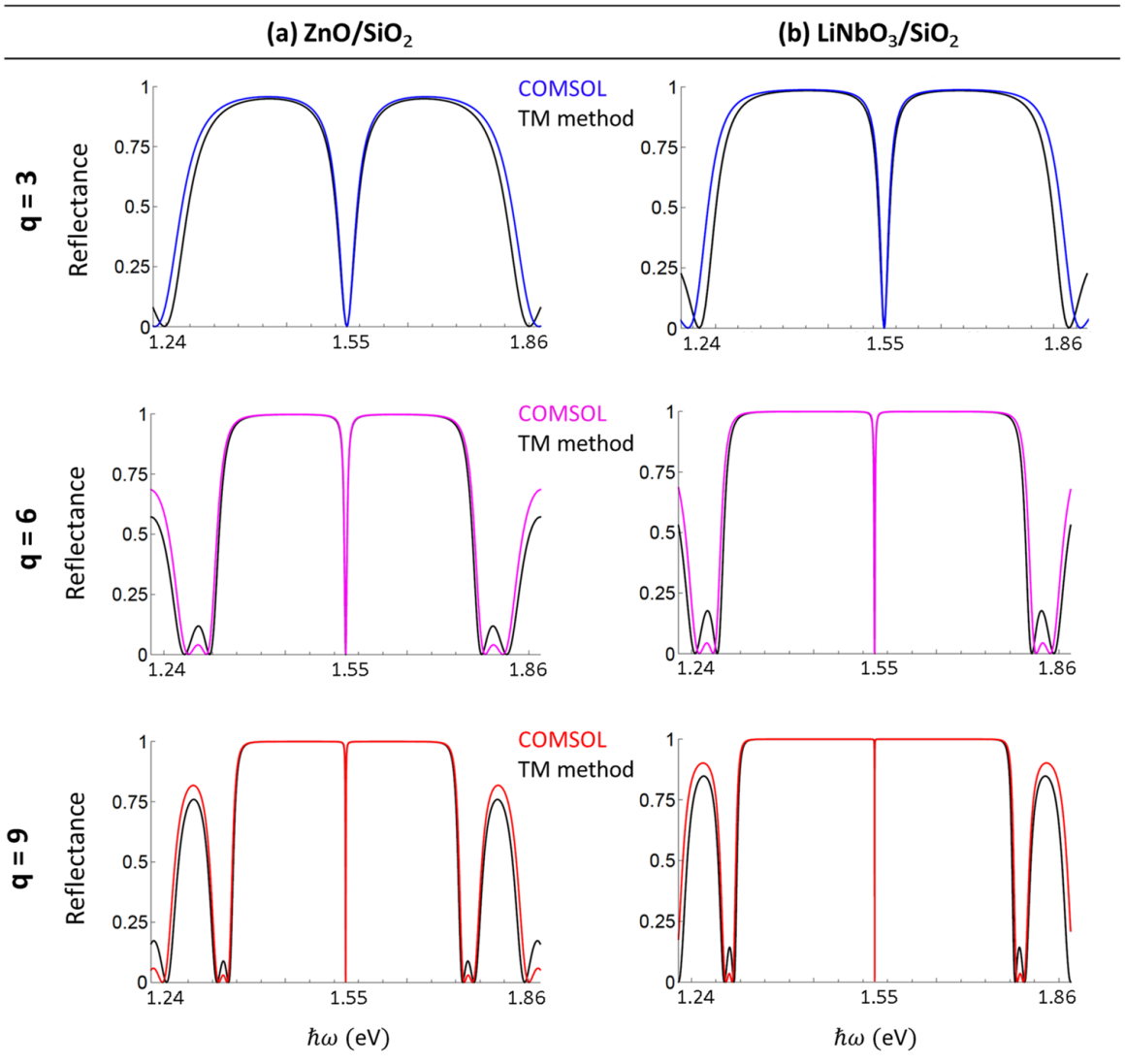

Figure 3.12: reflectance curves for both ZnO/SiO_2 (left column) and $LiNbO_3/SiO_2$ (right column) POMCs. The colored curves were obtained via COMSOL Multiphysics modelling, while the black ones were obtained via TM method calculations performed in Wolfram Mathematica. Each row and color is associated to a certain number of BM pairs, q. From top to bottom, $q = 3$ (blue), 6 (magenta), and 9 (red). The horizontal scales are expressed in terms of energy, in eV units, where the cavity resonance energy is $\hbar\omega_0 = 1.5498$ eV.

Figure 3.12 exhibits the reflectance curves for both ZnO/SiO_2 and $LiNbO_3/SiO_2$ POMCs with three different pairs of BMs: $q = 3, 6, 9$. As we observe, the PBGs are not fully formed when $q = 3$ (blue curves): the reflectance maxima are about 0.96 in ZnO, and 0.98 in $LiNbO_3$,

while resonance valleys are still broad. The estimated Q-factors for $q = 3$ are $Q = 45$ for ZnO, and $Q = 81$ for $LiNbO_3$, respectively. Advancing to $q = 6$ (magenta), it becomes noticeable that the PBGs have acquired a rectangular shape, with reflectance caps at 0.998 for ZnO, and ≈ 1.0 for $LiNbO_3$. The resonances have become more sharp, and the estimated Q-factors are $Q = 288$ and $Q = 881$ for ZnO and $LiNbO_3$, respectively. Finally, the red curves describe the $q = 9$ POMCs, which present fully-shaped rectangular PBGs and very sharp resonances. The estimated Q-factors in this case are $Q = 1972$ for ZnO, and $Q = 9370$ for $LiNbO_3$. The bandwidths of the PBG obtained for ZnO and $LiNbO_3$ are, approximately, $(\Delta f)_{ZnO} = 9 \times 10^{13}$ Hz and $(\Delta f)_{LiNbO3} = 1.1 \times 10^{14}$ Hz, respectively. In energy scale, these values correspond to 0.3722 eV and 0.4549 eV, respectively.

A good agreement between COMSOL (coloured curves) and the TM method (black curves) is observed, specially for higher qs. The small discrepancy between the two methods, which is more evident outside the photonic bandgap, has been attributed to the difference between the quality of the FEM discretization for each q. In COMSOL simulation, the mesh settings are study-controlled and the size of each element is not linearly scaled with q. Better agreement can be easily found by decreasing the element size in the simulation, which would require more computational effort. A summary of the Q-factors analysis obtained using COMSOL is presented in Figure 3.13.

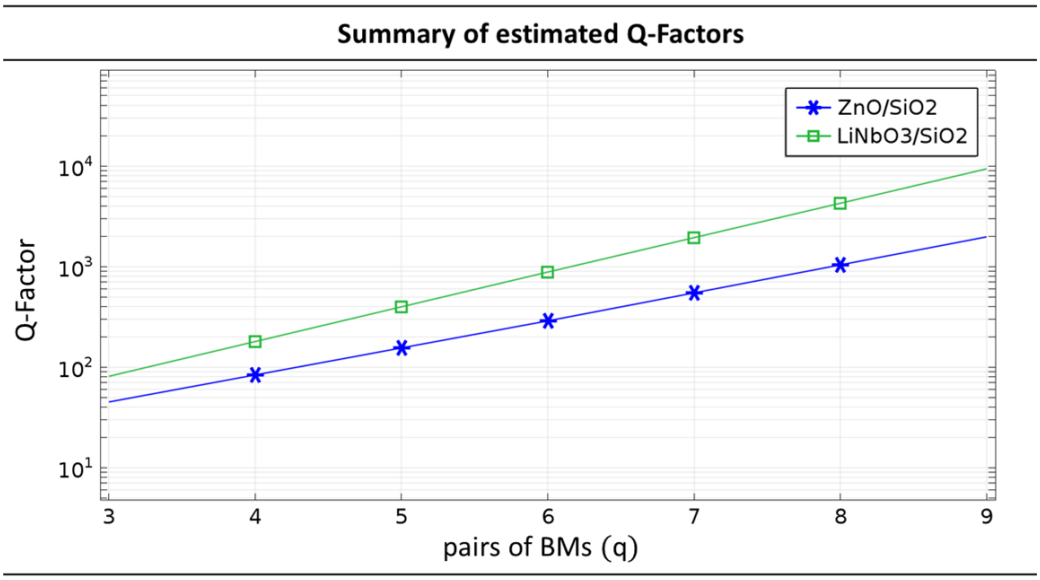

Figure 3.13: Q-factor dependence on q for both ZnO/SiO_2 and $LiNbO_3/SiO_2$ POMCs.

The resonant optical modes obtained with COMSOL are shown in Figure 3.14. In (a), a transversal cut line parallel to x_3 shows the electric field (blue), which presents maximum amplitude inside the cavity region and decays exponentially as $|x_3|$ increases. Even though the fields are normalized, their decay profile indicates that $LiNbO_3/SiO_2$ POMCs can more

effectively confine light inside as compared to ZnO/SiO_2 ones, as expected from the Q-factor. The 2D distribution of the electric field is presented in Figure 3.14(b). It shows that modes obtained from COMSOL calculations are indeed extended 2D-modes, as expected for the case of an infinite 2D POMC.

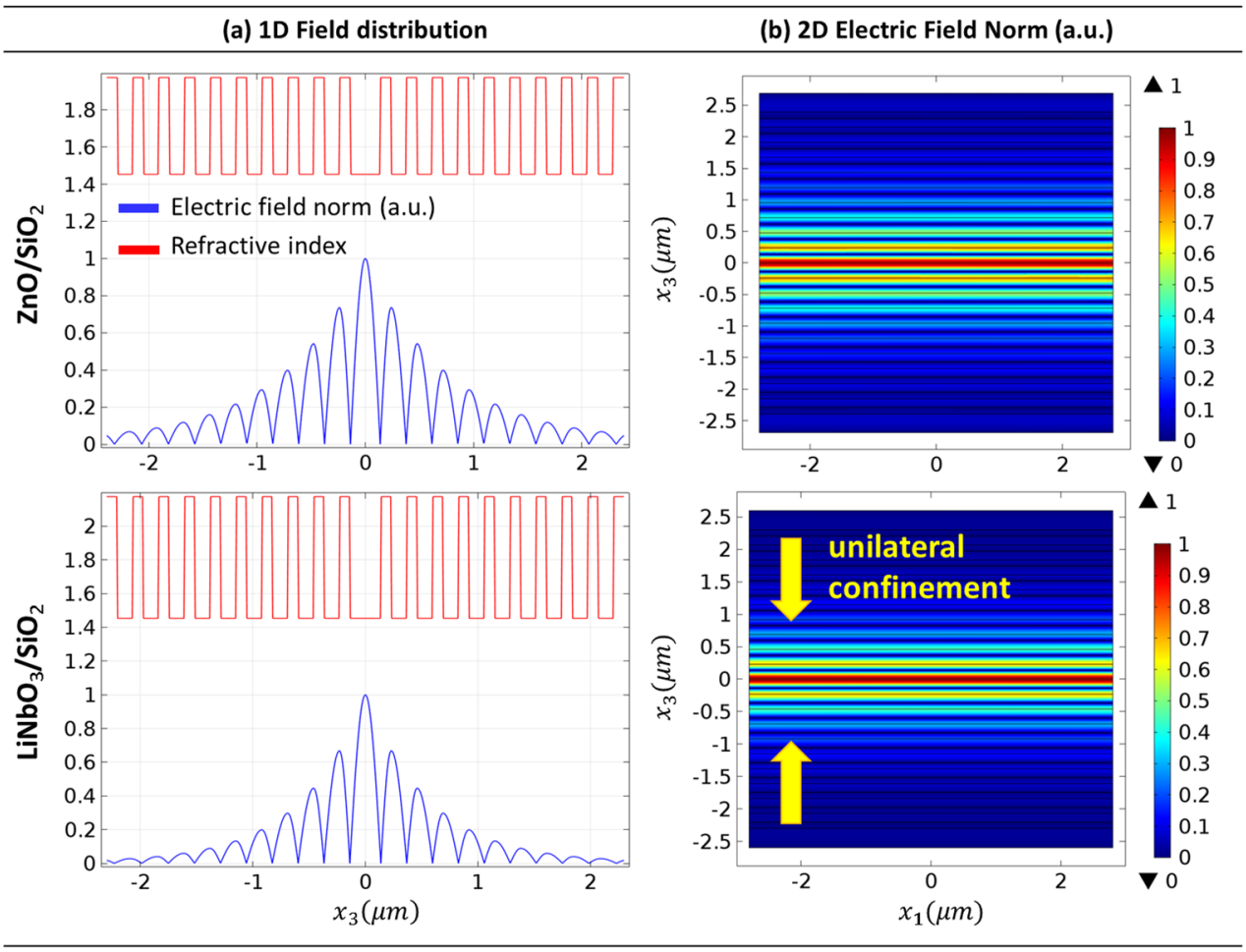

Figure 3.14: normalized electric field profiles at the cavity resonance frequency, $f_0 = 374.7$ THz, for POMCs containing $q = 9$ pairs of BMs. (a) 1D plots for the electric field norm (blue) and refractive index (red) along the x_3 direction; (b) 2D color plots for the electric field norm.

Finally, increasing the angle of light incidence at Port 1 allows us to obtain the photon dispersion of a POMC, which is described by the quadratic dispersion relation given by [24]

$$\hbar\omega = \hbar\omega_0\sqrt{1 + [k_1/(n_c k_3)]^2}, \tag{3.31}$$

where $\hbar\omega_0 = 1.5498$ eV is the cavity resonance energy, and k_1 and k_3 are the longitudinal and transversal components of the wave vector of light which are related by

$$\tan\theta = \frac{k_1}{k_3}, \tag{3.32}$$

where θ is the angle of light incidence defined with respect to the x_2Ox_3 plane.

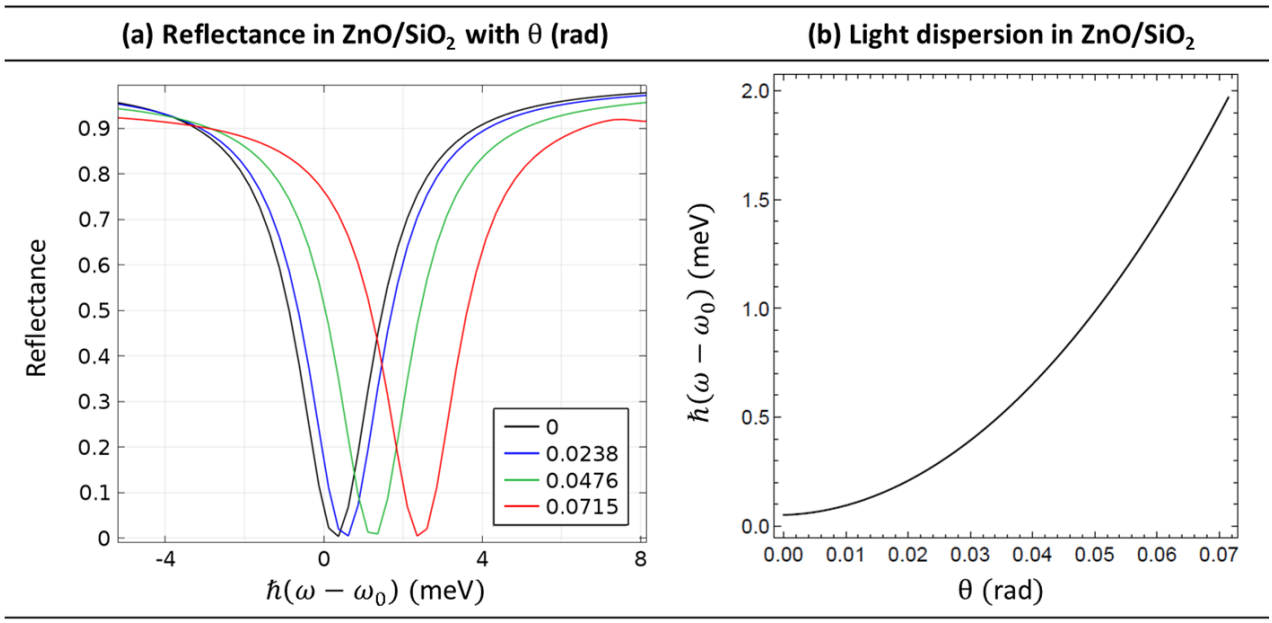

Figure 3.15: (a) near-resonance region of the reflectance curve for the 9-period ZnO/SiO_2 POMC at several oblique incident angles, θ. (b) Light dispersion, obtained via COMSOL, for such a structure with respect to θ.

By evaluating the reflectance spectrum for different light incidence angles we are, therefore, able to obtain the values of $\hbar\omega$ as a function of θ. We performed this calculation for the ZnO-based structure (the $LiNbO_3$-based one is analogous). The result is presented in Figure 3.15(a), where we have now more conveniently plotted the reflectance as function of light energy with respect to the cavity resonance energy $\hbar\omega_0 = 1.5498$ eV. As observed, the cavity resonance shifts towards higher energies (blue shift) as θ increases due the non-zero values of k_1. At the same time, the height of the PBG is reduced. Registering the position of each resonance valley and interpolating data points, we get the light dispersion of the POMC, shown in 3.15(b), which is indeed quadratic, as expected from equation 3.31.

We conclude this chapter by arguing that this model has successfully met its purposes. We have shown to be able to characterize the optical properties of POMCs, where the reflectance curves were evaluated for many different material structures in very good agreement with the analytical predictions from the TM method.

We could also estimate the Q-factor for these structures, which, in the particular case of ZnO-based POMCs, agree with experimental results (not presented here). We could also construct the quadratic dispersion relation for photons inside the POMC.

In the next chapter, we'll be addressing the effects on these results a SAW-induced strain field produces.

Chapter 4

SAW induced acousto-optic modulation

4.1 Introduction

The acousto-optic effect is the interaction mechanism between light and acoustic waves in solids. A starting point to understand this interaction lies in the definition of refractive index:

$$n \equiv \frac{c}{\eta}, \tag{4.1}$$

where η is the speed of light inside the solid. If we intuitively define a *mean free optical path* (MFOP) as the average distance that light can freely propagate without encountering any particles of the medium, we expect that materials which present high MFOPs and, thus, lower particle densities, also present $\eta \to c$ inside them, that is,

$$\uparrow \eta \iff \downarrow \rho, \tag{4.2}$$

where ρ is density. According to definition 4.1, this means that the refractive index must be somehow proportional to the density of particles, i.e.,

$$\uparrow n \iff \uparrow \rho. \tag{4.3}$$

In fact, reference [39] approaches this topic more quantitatively. In this way, relation 4.3 suggests the possibility of inducing changes to the refractive index of a certain device or material by changing its mechanical properties. As we have seen in section 2.2.1, when an acoustic wave propagates in solids, it forces particles of the medium to displace themselves, which culminates on the definition of strain (equation 2.12). It is this acoustically driven displacement the one responsible for changing the density of particles of the medium. As an example, Figure 4.1 illustrates a SAW deforming a dielectric layer as it propagates, inducing regions where particles become more separated (tension) and others where these become closer to each other (compres-

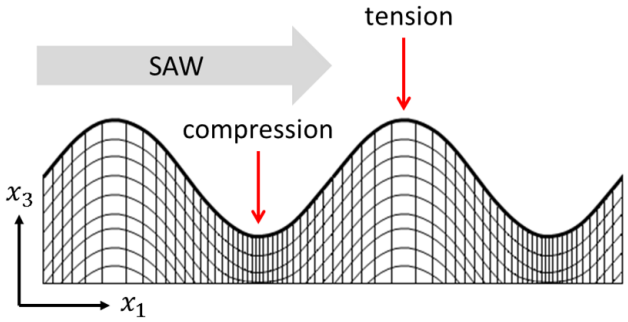

Figure 4.1: illustration of an acoustic wave that is propagating along the surface of a dielectric layer. The wave induces the formation of regions of increased (compression) and decreased (tension) particle densities.

sion). In those regions, the electronic and optical properties of the solid are thus being modulated; the former due to the piezoelectric fields, and the latter due to the mechanism expressed by relation 4.3. When a light beam whose width is larger than the SAW wavelength is incident on the solid (as illustrated in Figure 4.2), it "sees" a periodic array of refractive indexes and it gets diffracted.

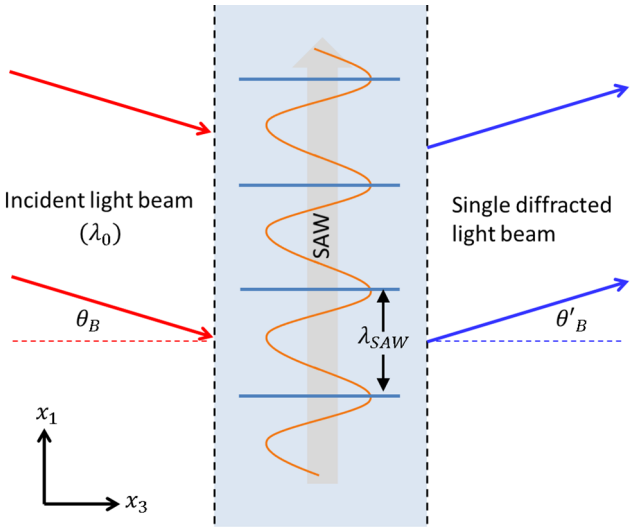

Figure 4.2: schematic representation of a Bragg modulator, where SAW wavefronts are diffracting light beams incident at the Bragg angle (θ_B) into one single light beam.

During the course of this chapter, we'll be discussing the relevant physical aspects of the acousto-optic modulation effect, and dedicate the final section to the presentation of our SAW + POMC coupled simulation model developed in the COMSOL Multiphysics platform, with interesting results being exhibited and discussed in the sequence.

4.2 The acousto-optic tensor

We begin by mathematically addressing the first order variation of the refractive index due to an arbitrary external influence. In the absence of any kind of disturbance, equation 4.1 can be written as [1]

$$n = \sqrt{\epsilon^r \mu^r}, \tag{4.4}$$

where ϵ^r and μ^r are relative permittivity and magnetic constant of the solid, respectively. Assuming the solid to be non-magnetic, the approximation $\mu^r \approx 1$ holds. Thus, equation 4.4 becomes

$$n = \sqrt{\epsilon^r}. \tag{4.5}$$

For simplicity, we're omitting the upper index from now on. When applying a small disturbance to the solid, i.e., the strain associated to the propagation of a SAW, the outcome is that both ϵ and n are affected:

$$n + \Delta n = \sqrt{\epsilon + \Delta\epsilon}; \tag{4.6a}$$

$$= \sqrt{\epsilon\Big(1 + \frac{\Delta\epsilon}{\epsilon}\Big)} \approx \sqrt{\epsilon}\Big(1 + \frac{\Delta\epsilon}{2\epsilon}\Big), \tag{4.6b}$$

where we have performed a first order Taylor expansion. The following relation can now be identified:

$$\Delta n = \frac{\Delta\epsilon}{2n}. \tag{4.7}$$

In anisotropic solids, the dielectric properties are conveniently expressed in terms of the refractive index ellipsoid, which is described by equation 4.8 and depicted in Figure 4.3 [1].

$$\left(\frac{x_1}{n_1}\right)^2 + \left(\frac{x_2}{n_2}\right)^2 + \left(\frac{x_3}{n_3}\right)^2 = 1, \tag{4.8}$$

where n_1, n_2 and n_3 are the principal indexes, i.e., the three semi-axes of the ellipsoid. Equation 4.8 may be written in terms of the impermittivity tensor, B_{ij}, as

$$B_{ij} x_i x_j = 1; \tag{4.9a}$$

where B_{ij} is defined as the inverse of the relative permittivity tensor:

$$\epsilon_{ki} B_{ij} = \delta_{kj}. \tag{4.9b}$$

The set of equations 4.9(a-b) provides [1]

$$\Delta\epsilon_{kl} = -\epsilon_{ki} \Delta B_{ij} \epsilon_{jl}. \tag{4.10}$$

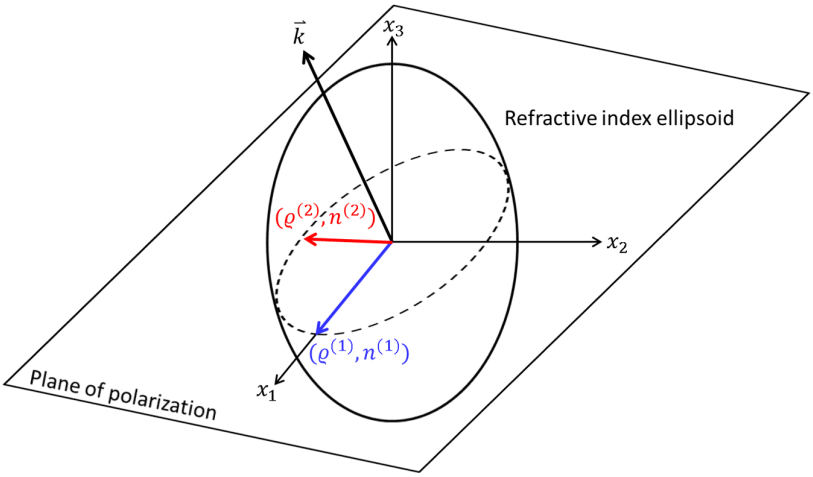

Figure 4.3: the refractive index ellipsoid for an anisotropic solid. A light beam with wave vector $\vec{k}$ may be polarized along $\varrho^{(1)}$ or $\varrho^{(2)}$, which lie in the same plane. These polarizations are usually not aligned with the principal axis, and the propagation velocity is determined by the off-diagonal terms $n^{(1)}$ and $n^{(2)}$ according to equation 4.1.

Thus, writing equation 4.7 in terms of the impermittivity gives

$$\Delta n_{kl} = \frac{-\epsilon_{ki}\Delta B_{ij}\epsilon_{jl}}{2n_{kl}}. \tag{4.11}$$

Relation 4.3 and equation 4.11 are consistent assuming that the refractive index ellipsoid is, somehow, related to acousto-optic modulation phenomena. In fact, this relation is given by [1]

$$\Delta B_{ij} = p_{ijkl}S_{kl}. \tag{4.12}$$

where p_{ijkl} is the fourth-rank acousto-optic tensor, also known as the Pockels tensor. It is an dimensionless physical quantity that mediates the coupling between light and acoustic waves in solids. It follows that such a tensor must be related to the crystalline structure of solids and, similarly to the stiffness tensor (c_{ijkl}), it can be written in reduced notation. Tables A.5 and A.6 from the Appendix exhibit the acousto-optic tensors and constants for several materials in such notation. A vast library can be found in reference [22].

4.2.1 The electro-optic effect

The application of an electric field to a solid can modify its refractive index ellipsoid via the *electro-optic effect* [1, 21, 22]:

$$\Delta B_{ij} = r_{ijp}E_p, \tag{4.13}$$

where r_{ijp} is the third-rank electro-optic tensor. Typically expressed in units of pm/V, this physical quantity mediates the mechanical deformation of materials due to electric and piezo-

electric (as in piezoelectric solids) perturbations.

The electro-optic effect is responsible for the *indirect acousto-optic effect*, where it contributes to the Pockels tensor according to equation 4.14 [1]:

$$p^*_{ijkl} = p_{ijkl} - \frac{r_{ijp}\hat{n}_p\hat{n}_q d_{qkl}}{\epsilon_0 \epsilon_{jk}\hat{n}_j\hat{n}_k}, \tag{4.14}$$

where p^*_{ijkl} and p_{ijkl} are the *effective* and *direct* acousto-optic constants, and $\hat{n}_{p,q,j,k}$ is the unit vector along the SAW propagation direction.

The literature typically reports the effective acousto-optic constants. For most piezoelectric materials, however, the electro-optic effect is very small [21], being $LiNbO_3$ one of the exceptions with a particularly strong effect along the x_3 direction. Our models account for the electro-optic effect.

4.2.2 Acousto-optic modulation induced by SAWs

Figure 4.4 illustrates the system of our interest. A POMC with aluminium IDTs deposited over its surface has been placed on top of a sapphire substrate - a hard and transparent crystal

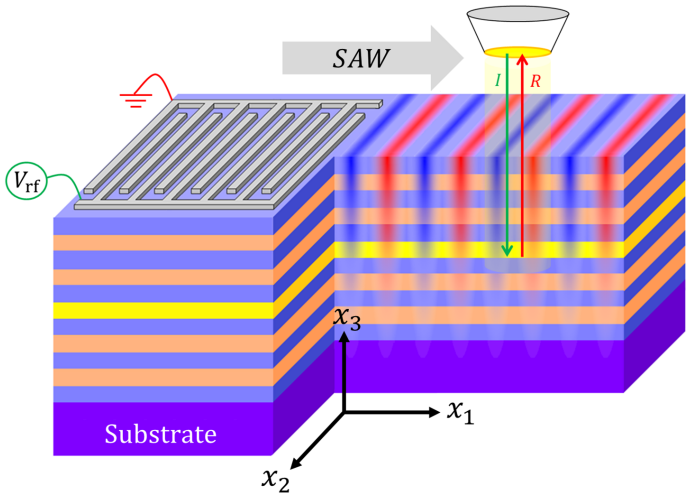

Figure 4.4: representation of a POMC being modulated by a SAW. The former is deposited on top of a sapphire substrate and the IDTs on its surface are generating Rayleigh SAWs along x_1. At the same time, a reflectivity measurement is being performed. The SAW-induced strain field deforms the POMC geometry and the regions of compression and tension are represented in red and blue, respectively.

that shifts SAW modes to higher frequencies (thus, higher SAW velocities). As the IDTs vibrate due to the converse piezoelectric effect, SAWs are being launched towards the x_1 direction. At the same time, reflectivity measurements are being performed.

The SAW-induced strain field is responsible for modulating not just the refractive index of the whole device, but also the physical thickness of each layer. The effective cavity modulation, for example, can be expressed as [27]

$$\frac{\Delta\omega_0}{\omega_0}\Big|^{(\varrho)} \approx -\Big[\frac{\Delta d_c}{d_c} + \frac{\Delta n_c}{n_c}\Big|^{(\varrho)}\Big] = -\Big[S_{33} + \frac{\Delta n_c}{n_c}\Big|^{(\varrho)}\Big], \tag{4.15}$$

where ϱ is the polarization of light. In this work, however, we're assuming light to be TE-polarized (i.e., $\varrho = x_2$). Therefore, we are not addressing the effects of light polarization in this dissertation.

Equation 4.15 suggests that the S_{33} strain field component is most relevant here. The refractive index modulation term ($\Delta n_c/n_c$) can be derived from equations 4.11 and 4.12 for a SiO_2 layer, which gives

$$\frac{\Delta n_c}{n_c} = -\begin{bmatrix} \frac{\epsilon^2}{2n}(p_{11}+2p_{12})S_{11} & 0 & \frac{\epsilon^2}{2n}(p_{11}+2p_{12})S_{13} \\ 0 & 0 & 0 \\ \frac{\epsilon^2}{2n}(p_{11}+2p_{12})S_{13} & 0 & \frac{\epsilon^2}{2n}(p_{11}+2p_{12})S_{33} \end{bmatrix}, \tag{4.16}$$

where we have used the information contained in Tables A.4 and A.5 from the Appendix, and the fact that $S_{12} = S_{22} = S_{23} = 0$ for Rayleigh SAW modes. Equation 4.16 shows us that both terms from equation 4.15 are, in fact, dependent on the strain field inside the cavity.

As for the piezoelectric layers, equations 4.11 and 4.12 provide a slightly more complicated expression:

$$\frac{\Delta n_{kl}}{n_{kl}} = -\frac{1}{2n_{kl}}\begin{bmatrix} \epsilon_1[\epsilon_1(p_{11}+p_{12})+\epsilon_3 p_{13}]S_{11} & 0 & \epsilon_1[\epsilon_1(p_{11}+p_{12})+\epsilon_3 p_{13}]S_{13} \\ 0 & 0 & 0 \\ \epsilon_3(2\epsilon_1 p_{31}+\epsilon_3 p_{33})S_{13} & 0 & \epsilon_3(2\epsilon_1 p_{31}+\epsilon_3 p_{33})S_{33} \end{bmatrix}. \tag{4.17}$$

In this way, each material layer will be acoustically modulated according to expressions 4.15, 4.16 and 4.17. By making use of these equations, we have everything we need to develop the SAW + POMC coupled model, to be introduced in the next section.

4.3 The acousto-optic simulation model

This final simulation model is achieved by merging the previous models from chapters 2 and 3. Thus, a rather simple explanation will be now sufficient to fully describe it.

The simulation geometry is being presented in Figure 4.5, where we have a 9-period, 800nm POMC on top of a 300nm-thick sapphire substrate. Over the POMC, we have two 1×0.2 μm aluminium IDTs covered by a 300nm-thick top air layer. The width of this "unit cell" is the SAW wavelength, $\lambda_{SAW} = 5.6$ μm. The inset of Figure 4.5 describes each geometric entity,

material composition and layer thickness.

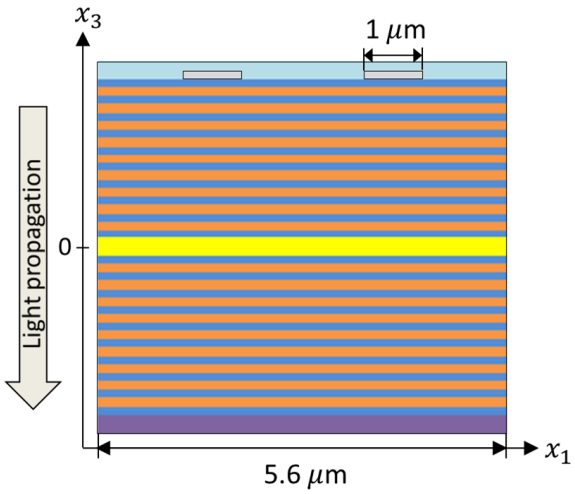

Material	Geometry	Thickness (nm)
Air	Top cover	300
Aluminium	IDTs	200
ZnO	High ref. index layer	101.32
$LiNbO_3$		91.95
SiO_2	Low ref. index layer	137.65
SiO_2	Cavity	275.29
Sapphire	Substrate	300

Figure 4.5: geometry under study by the acousto-optic coupling model. Inset: material composition, geometric entities and layer thicknesses.

All boundary conditions from sections 2.4 and 3.6 have been applied to this model. The acousto-optic effects were included by imposing equations 4.16 and 4.17 to the refractive index of each material ($n \rightarrow n + \Delta n$).

Two observations must be made here: i) in order to maintain the same optical configuration as the optics model (section 3.5), the refractive indexes of the substrate and the IDTs have been set to unity ($n_{IDTs} = n_{sapph} = 1$); ii) a 300nm-thick sapphire substrate has been verified to provide enough acoustic damping to our needs, practically acting as a PML. The simulation procedure is held according to the following algorithm:

1) Perform acoustic frequency sweeps in order to obtain the modes whose strains are the highest among all the others in the scan range inside the cavity region (as in section 2.4.1);

2) Seek for eigenmodes around the frequencies obtained in the previous step. Each eigenmode provides different strain profiles, which, according to equation 4.12, modulates the dielectric properties of the POMC in different ways;

3) For each of these strain profiles, perform optical frequency scans to obtain the modulated spectral curves of reflectance (as in section 3.6.1).

4.3.1 Characterization of SAW modes in POMCs

Performing step 1 within the frequency range comprised between 500 and 1200 MHz provides three prominent acoustic resonances for each ZnO/SiO_2 and $LiNbO_3/SiO_2$ POMCs. These

are exhibited in Figures 4.6(a) and (b), respectively. The position of resonances from Figure 4.6(a) were verified to be in good agreement with experimental data for ZnO/SiO_2 POMCs [38].

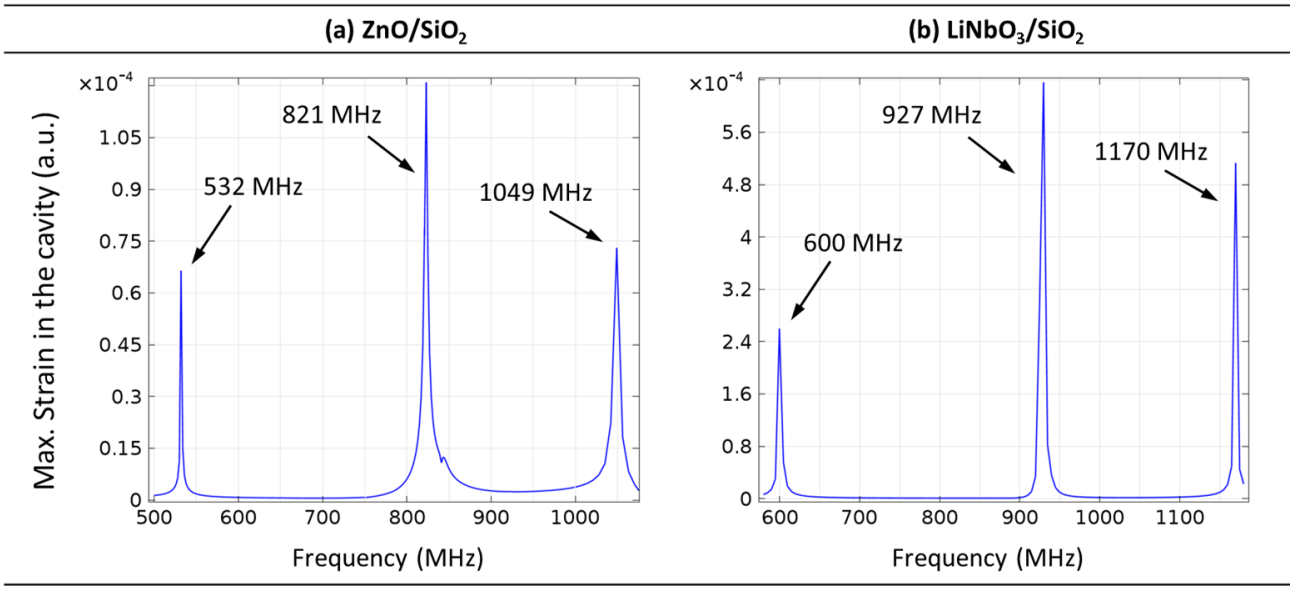

Figure 4.6: frequency sweeps for the maximum total strain amplitude values (expressed in arbitrary units) inside the optical cavity. In (a), the results are shown for the ZnO/SiO_2 POMC. In (b), those for the $LiNbO_3/SiO_2$ POMC are exhibited. Three prominent acoustic resonances were obtained in each case.

Each resonance from Figure 4.6 is expected to be a Rayleigh SAW mode. The relative comparison between their strain amplitudes, however, has to be performed by using the eigenfrequency study step, as our model does not include acoustic damping, heat dissipation losses, etc. That could be masking the amplitude of our results, and further investigation is thus required. Therefore, by performing step 2, we get to analyze the eigenmodes corresponding to these resonances. Figure 4.7 presents 2D color plots of the S_{33} strain field component for each eigenmode obtained around the frequency position expected from Step 1. Here, we attest that these are indeed Rayleigh SAW eigenmodes, where differences between one another lies in their propagation velocities, number of nodes and maximum amplitude.

Each eigenmode seems to present relevant strain amplitudes in the cavity, because the nodes have appeared in the region where the BMs are. However, to address this more properly, we shall evaluate the acoustic penetration profiles along x_3 by performing vertical cut-lines below the left IDT (the case for the right IDT is analogous). Our particular interest here lies on these profiles for the refractive index modulation (which, according to equations 4.16 and 4.17, is linearly proportional to the strain, thus inheriting its shape) and the piezoelectric field (for studies in semiconductor systems). The results are presented in Figure 4.8, where we have plotted the refractive index modulation $(\Delta n/n)_3$ and the E_3 piezoelectric field component along

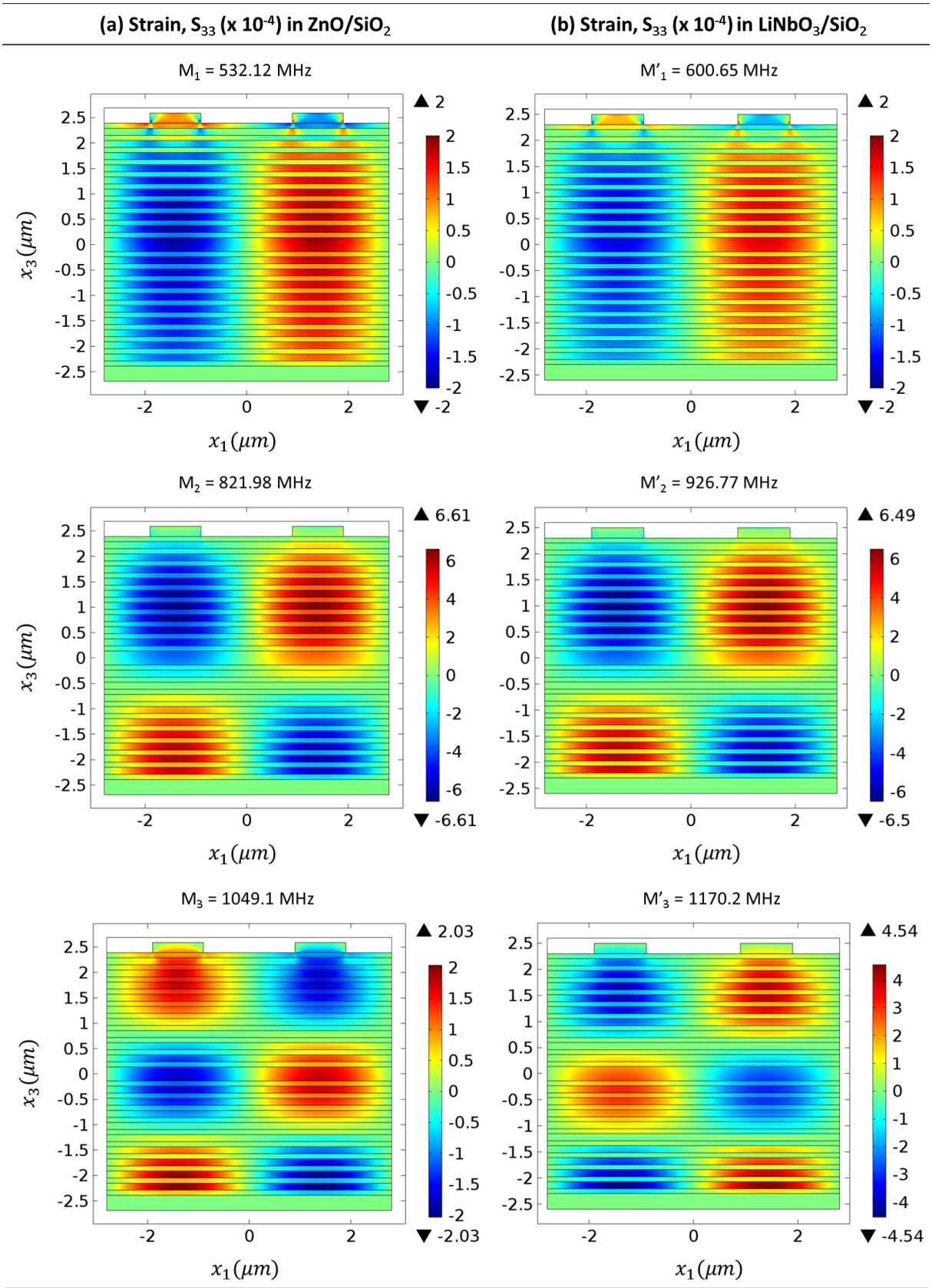

Figure 4.7: 2D color plots for the strain field (S_{33} component) for three distinct Rayleigh SAW eigenmodes inside the (a) ZnO/SiO_2 and (b) $LiNbO_3/SiO_2$ POMCs.

the periodicity of both (a) ZnO and (b) $LiNbO_3$-based POMCs. The inset depicts the vertical cut-line.

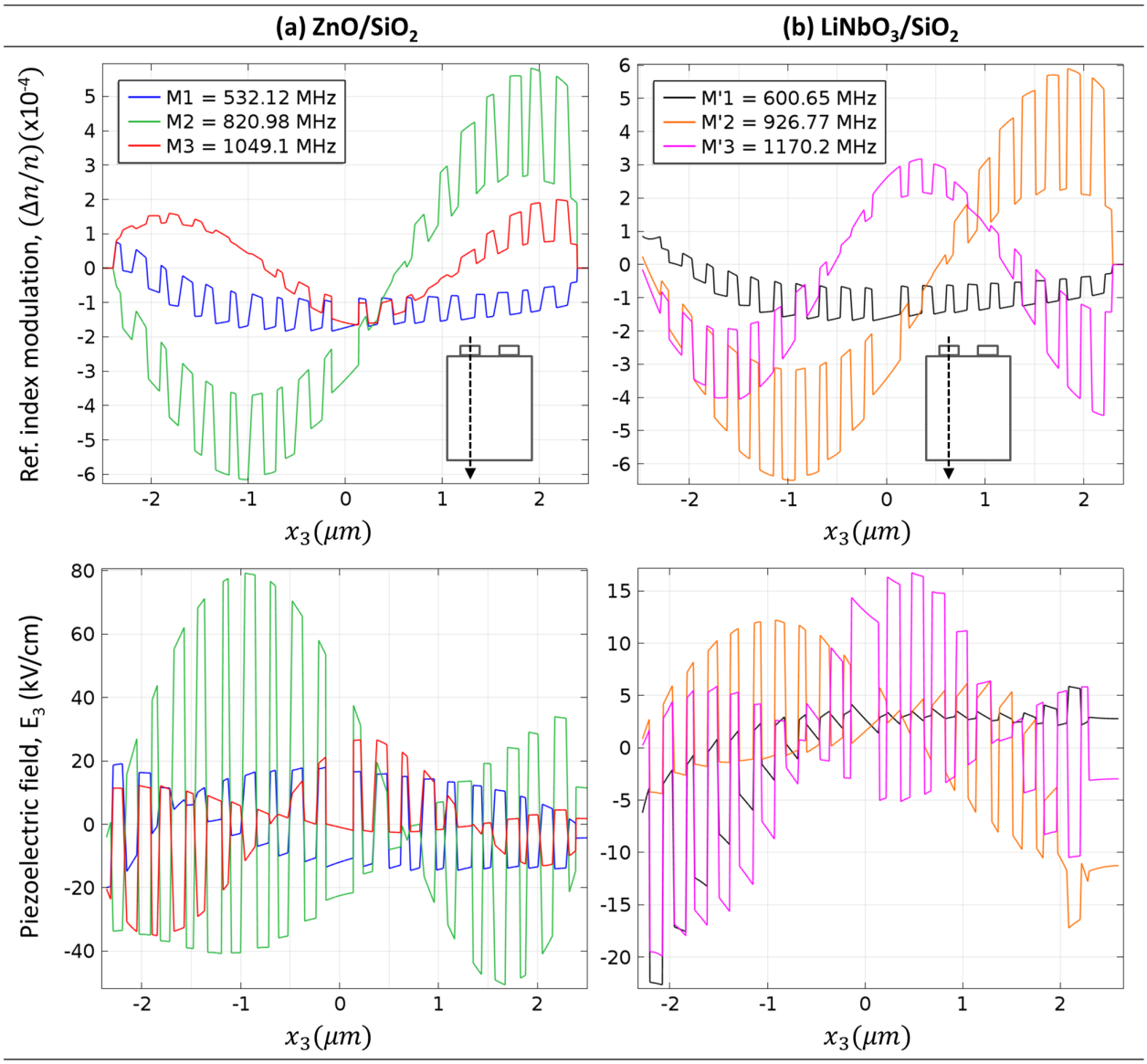

Figure 4.8: refractive index modulation ($\Delta n/n$) and piezoelectric field (E_3 component) profiles inside the (a) ZnO/SiO_2 and (b) $LiNbO_3/SiO_2$ POMCs for three distinct Rayleigh SAW eigenmodes. Inset: vertical cut-lines performed to obtain such profiles.

In Figure 4.8(a), we observe that the $M_2 = 820.98$ MHz (green) mode is responsible for both maximum refractive index modulation ($\approx 3 \times 10^{-4}$) and piezoelectric field (≈ 22 kV/cm) amplitudes in the cavity layer. The magnitude of this modulation is very similar to what is typically achieved in experiments, as demonstrated by our references [24, 38]. In Figure 4.8(b), the $M'_2 = 926.77$ MHz (orange) is the one that leads to the highest refractive index modulation ($\approx 3.5 \times 10^{-4}$, top of Figure). However, it can be seen on the bottom of this Figure

that its piezoelectric field amplitude is very small in the cavity active layer ($\approx$ 2 kV/cm). In semiconductor systems, it would be much more interesting to be working with modes that present high piezoelectric field amplitudes. Mode M_3' = 1170.2 MHz (magenta) presents a relatively high refractive index modulation ($\approx 2.5 \times 10^{-4}$) and also a strong piezoelectric field ($\approx$ 12.5 kV/cm) in the cavity layer. In this way, the M_2 and M_3' modes have been selected. We shall now address how these modes affect the optical response of POMCs.

4.3.2 SAW-induced optical superlattices

After choosing some of the acoustic modes to be focusing on, we begin to address the acoustically induced changes to the optical properties of POMCs.

The refractive index modulation distribution of the M_2 and M_3' acoustic modes for ZnO/SiO_2 and $LiNbO_3/SiO_2$ POMCs, respectively, is presented in more detail in Figure 4.9. The modulation is maximum close to the middle of the Bragg mirrors and follows approximately the strain distribution of the S_{33} components.

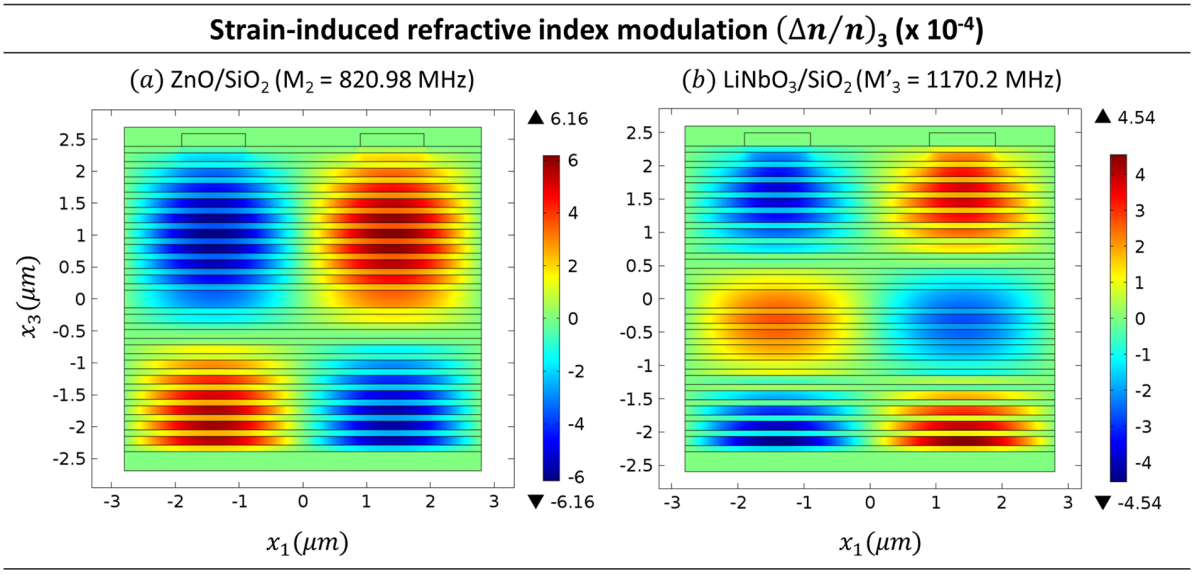

Figure 4.9: 2D color plots for the refractive index modulation $(\Delta n/n)_3$ in (a) ZnO/SiO_2 and (b) $LiNbO_3/SiO_2$ POMCs for the M_2 and M_3' Rayleigh SAW eigenmodes, respectively.

In order to simulate the effects of acoustic power on the optical properties, we introduce the *strain multiplier* parameter, β. It is defined as

$$S'_{kl} = \beta S_{kl}, \tag{4.18}$$

where S'_{kl} and S_{kl} are the renormalized and normalized (eigenmode solution) strains, respectively. We call it "strain multiplier" to avoid confusion in terminology with the actual (experi-

mental) acoustic power. By varying β, this definition allows us to change the amplitude of the strain field S'_{kl} in the structure, which is then used as an input to step 3, defined in section 4.3. In this way, we are able to calculate the optical response of POMCs under controlled strain magnitudes. This parameter also permits us to compare the behaviour of ZnO and $LiNbO_3$-based structures when subjected to similar strains. In fact, this is presented in Figure 4.10, where we have evaluated the reflectance in the near-resonance region for (a) ZnO/SiO_2 and (b) $LiNbO_3/SiO_2$ POMCs, for the same increasing strain amplitudes S'_{kl} (in the order of 10^{-3}), and under normal light incidence.

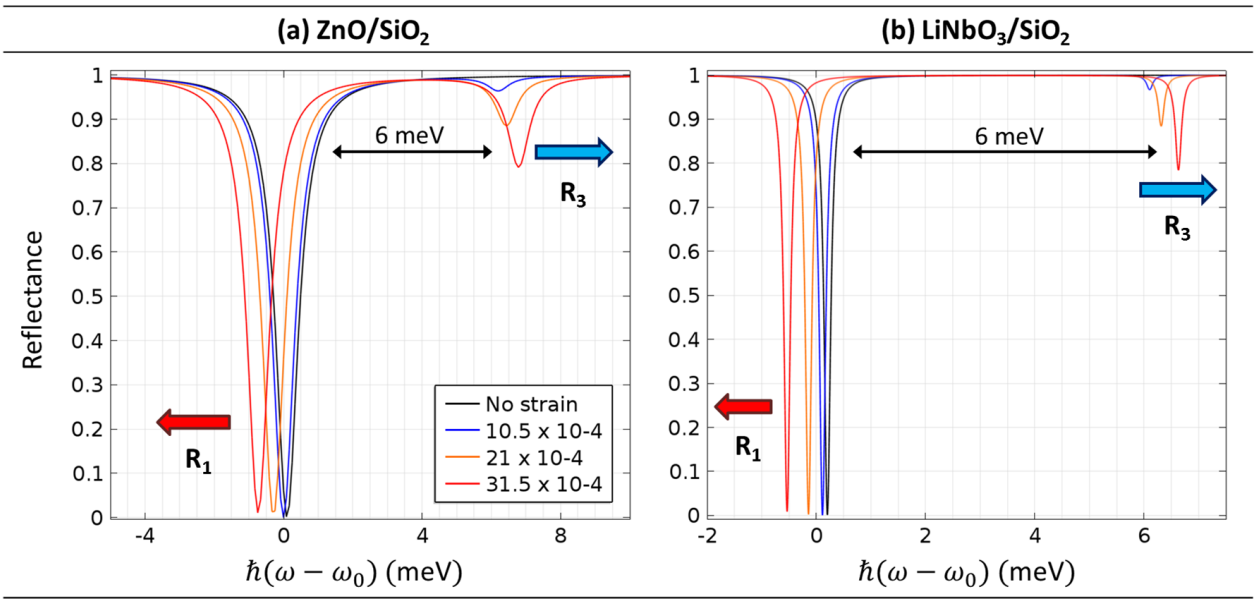

Figure 4.10: near-resonance reflectance spectrum for normal light incidence and varying cavity strain amplitudes in the (a) ZnO/SiO_2 and (b) $LiNbO_3/SiO_2$ POMC. The horizontal energy scales are relative to the cavity resonance energy $\hbar\omega_0 = 1.5498$ eV.

The black curves were obtained in the absence of a SAW. In this case, only the cavity resonance (R_1) is observed. Turning the SAW on causes two optical resonances to appear (R_1 and R_3), which are initially separated by approximately 6 meV. As the strain is increased, R_1 shifts to lower energies (red shift), while R_3 shifts towards higher energies (blue shift). The latter also becomes more pronounced. A reasonably high strain amplitude is necessary to observe the two resonances, which is one of the reasons why this effect has not been observed in experiments with ZnO/SiO_2 POMCs, where strains of about $\approx 2 \times 10^{-4}$ have been applied [38].

Figure 4.11 shows what happens to the reflectance spectrum of a POMC under a certain average strain amplitude in the cavity when the calculations are performed by varying the angle of light incidence, θ. As we observe, for $\theta > 0$, in all cases, another reflectance minimum (R_2) appears in between the ones previously observed under normal light incidence. Now, as θ is increased, R_3 blueshifts, R_2 redshifts, and R_1 slightly blueshifts. The behavior is the same

in both ZnO/SiO_2 and $LiNbO_3/SiO_2$ POMCs. Again, as the strain is increased, R_2 and R_3 become more pronounced (not shown in the case of Figure 4.11), reaching lower reflectance values.

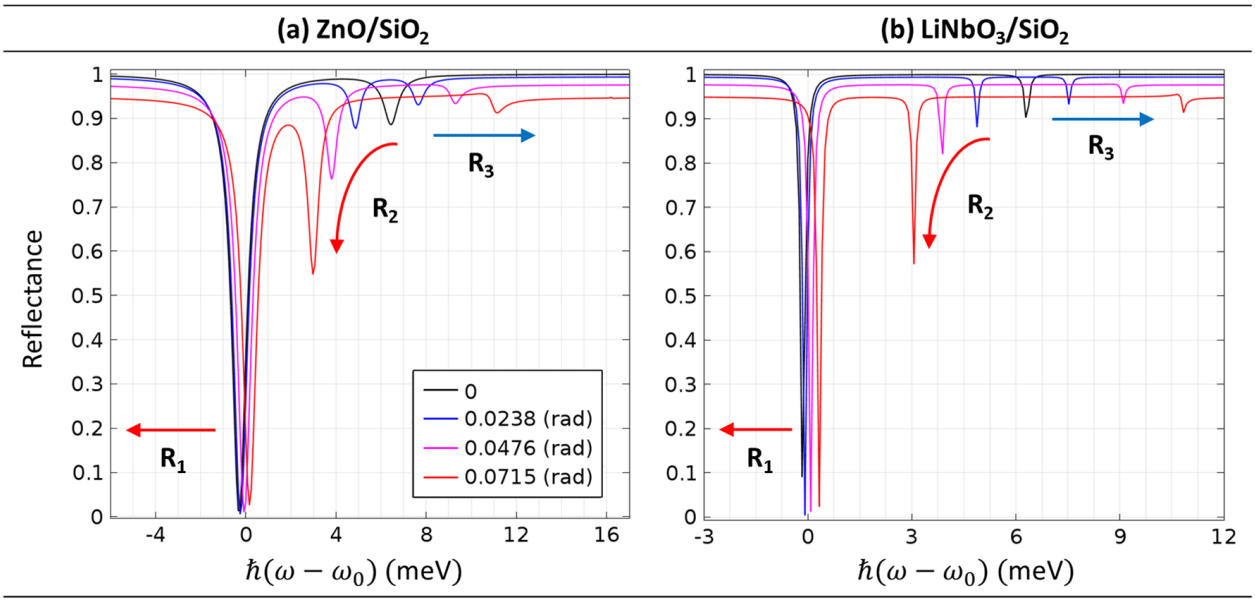

Figure 4.11: near-resonance reflectance spectrum for varying light incidence angles and fixed cavity strain amplitude ($S = 21 \times 10^{-4}$) in the (a) ZnO/SiO_2 and (b) $LiNbO_3/SiO_2$ POMC. The horizontal energy scales are relative to the cavity resonance energy $\hbar\omega_0 = 1.5498$ eV.

In order to understand the behaviour of these resonances under varying strain amplitudes and angle of light incidence, we've registered the position of each resonance as a function of θ for different average strain values. The result (after an interpolation of data points using Wolfram Mathematica) is presented in Figure 4.12 for both POMCs. The regime of vanishing strain amplitudes is represented by the thin black lines. Here, we write θ in terms of the ratio between the in-plane wave vector of light, k_1, and SAW wave vector, k_{SAW}. The vertical energy scales are relative to the cavity resonance energy: $\hbar\omega_0 = 1.5498$ eV.

Figure 4.12 basically exhibits what happens to light dispersion when the periodic modulation of a SAW is introduced in the system. The modulation period is determined by the SAW wave vector ($k_{SAW} = 2\pi/\lambda_{SAW}$) and light gets diffracted by this SAW-induced optical superlattice. The coupling between the light ($\vec{k}_0$) and SAW ($\vec{k}_{SAW}$) wave vectors is schematically depicted in Figure 4.13 along with the reflected beam ($\vec{k}_R$) in the extreme case where the vectorial sum $\vec{k}_0 + \vec{k}_R = \vec{k}_{SAW}$ holds ($\vec{k}_D$ represents the diffracted beam). For $\theta = 0$, the light beam has absolutely no longitudinal vector component ($\vec{k}_1$). On the other hand, a slight increase in θ is sufficient to provide the incident light beam with a small $\vec{k}_1$, and so it begins to "see" the superlattice.

The signature of the superlattice is the folding of the dispersion relation, observed in Fig-

ure 4.12, characterized by the appearance of "mini" Brillouin zones (MBZs). The boundaries of the MBZ correspond to $k_1/k_{SAW} = \pm 0.5$, but in Figure 4.12 we have plotted only the positive

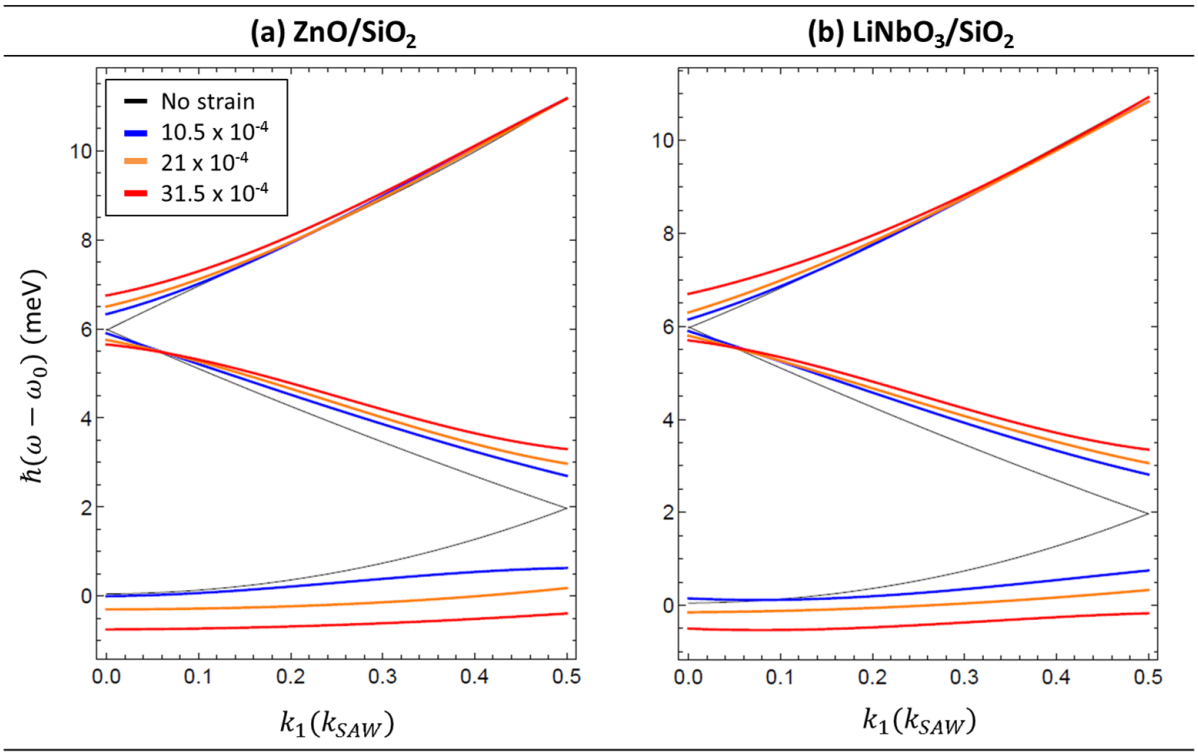

Figure 4.12: calculated light dispersions for the (a) ZnO and (b) $LiNbO_3$-based POMCs, and for several average strain amplitudes in the cavity. The vertical energy scales are relative to the cavity resonance energy $\hbar\omega_0 = 1.5498$ eV. Data points were interpolated using Wolfram Mathematica.

values of k_1 (the negative case is analogous). The right border of the MBZ is obtained when

$$\theta = \sin^{-1}\left(\frac{k_{SAW}}{2k_0}\right) \approx 0.0715 \text{ rad.} \tag{4.19}$$

Increasing the strain causes energy gaps to open up at the center ($k_1 = 0$) and at the right border ($k_1 = k_{SAW}/2$) of the MBZ (colored lines in Figure 4.12), which is consistent with the appearance of two shifting resonances in Figure 4.10 ($k_1 = 0$) and three shifting resonances in Figure 4.11 ($k_1 > 0$). The amplitude of these gaps lie in the range of a few meV, being slightly larger in the ZnO-based POMC when compared to the $LiNbO_3$-based one. This has been attributed to differences between the strain field distribution inside the cavity in each case (Figure 4.7). Furthermore, the behavior of the energy gap at the right edge of the MBZ, shown in Figure 4.12, is in very good agreement with the experimental results obtained in GaAs/AlGaAs POMCs as function of the applied acoustic power [24].

More information about the phonon-photon interaction can be extracted by looking into what happens to the electric field of light when the acoustic modulation is turned on. Figure 4.14

exhibits the electric field inside the $LiNbO_3/SiO_2$ POMC (the analogous case has been observed in the ZnO-based structure) when the average strain amplitude in the cavity is $S = 10.5 \times 10^{-4}$, and light is incident at angle $\theta = 0.0238$ rad (corresponding to $k_1 = k_{SAW}/6 \approx 0.167\ k_{SAW}$).

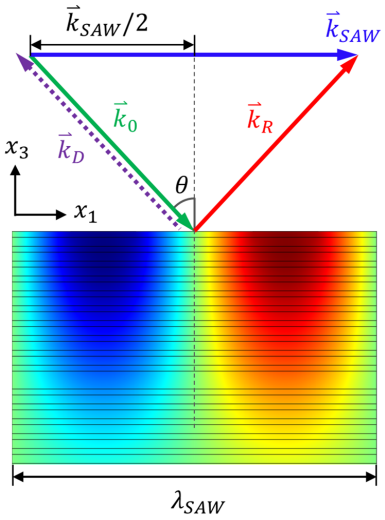

Figure 4.13: schematic representation of the acoustic and optic wave vectors in a configuration where a light beam is incident at an angle $\theta = 0.0715$ rad on the surface of a POMC when a SAW-induced optical superlattice is present.

The electric field distribution for the R_1 mode is presented in Figure 4.14(a), while the

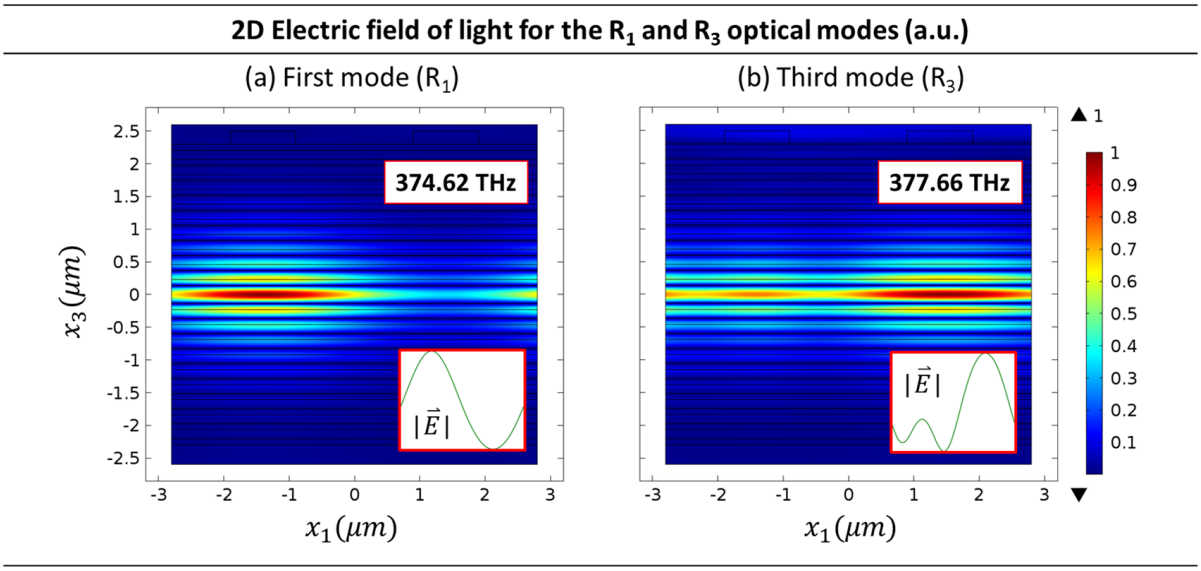

Figure 4.14: electric field distribution inside the 2D geometry of the $LiNbO_3/SiO_2$ POMC under the average strain amplitude of $S = 10.5 \times 10^{-4}$ and light incidence angle $\theta = 0.0238$ rad. The R_1 and R_3 modes are presented in (a) and (b), respectively. Insets: electric field norm along the $x_3 = 0$ horizontal line.

distribution for the R_3 mode is exhibited in Figure 4.14(b). In the absence of SAW modulation, the optical mode is confined only vertically (x_3 direction) in the cavity, as we have shown in Figure 3.14. In Figure 4.14(a), however, one observes that, for R_1, as the SAW is turned on, a lateral confinement of light towards the higher refractive index region of the cavity (see Figure 4.9) occurs. Confinement of light in the higher refractive index region of the active layer is consistent with the redshift observed for the lower energy mode as the strain is increased. Since the cavity resonance energy is given by $E_0 = hc/\lambda_0 = hc/2d_c n_c$, in regions of higher values of n_c the photon energy should be lower.

The same is valid for the R_3 mode. Figure 4.14(b) shows that the photonic wave function for this mode tends to be more confined in the lower refractive index region. In this region of the cavity, as the amplitude of the strain is increased, the refractive index decreases, thus leading to a blueshift of the cavity resonance, as observed in the dispersion curve presented in Figure 4.12.

Chapter 5

Conclusions

We have investigated the effects of acousto-optic modulation in planar optical microcavities (POMCs) due to the propagation of Rayleigh surface acoustic waves (SAWs). Our study has been based on computational simulations performed on the COMSOL Multiphysics platform, making use of the finite element method (FEM). During the course of this dissertation, we have presented the physical description of each individual subject (i.e., acoustic waves in piezoelectric solids and light confinement in POMCs) in order to unite them under the perspective of acousto-optics.

In the first part of this work, we have shown how to characterize the acoustic and piezoelectric properties of single crystal substrates, such as Zinc Oxide (ZnO) and Z-cut Lithium Niobate ($LiNbO_3$) by using our acoustics simulation model. We were able to determine the SAW generation frequencies in piezoelectric substrates and to obtain the propagation velocities, displacement amplitudes, strains, piezoelectric fields and potentials - all verified to agree well with literature reports. This simple model is open to about any choice of piezoelectric material, being applicable not just for SAWs, but rather any type of acoustic mode. The acoustics model can be particularly useful for applications in semiconductor nanosystems, where piezoelectric fields are used to transport and manipulate electrons, holes and photons.

In the second part, we have been successful in optimizing the design of POMCs and in characterizing their optical properties. We have designed several different structures consisted of either ZnO/SiO_2 or $LiNbO_3/SiO_2$ Bragg mirrors that sandwich a $\lambda_0/2$ SiO_2 optical cavity layer. The results obtained with this simulation model have shown to be in very good agreement to the transfer matrix method (TM), as well as experimental evidence found in the literature. We have shown that high Q-factors, exceeding 10^4, can be achieved (specially in $LiNbO_3/SiO_2$) due to the high refractive index contrast between Bragg mirror layers. Besides, our model also allows for light incidence at oblique angles. In this way, we were able to fully characterize the photon dispersion and show its quadratic behavior, as expected.

The previous models were successfully merged to address the acousto-optic interaction. We were able to completely characterize the coupling regime between photons trapped in the cavity and phonons due to the SAW propagation. We have shown that the optical resonances of POMCs can be tuned with SAW-induced strains, and how the strong coupling between photons and phonons leads to the formation of dynamic optical superlattices in our systems, which are responsible for folding the light dispersion into a "mini" Brillouin zone (MBZ). By tuning the strain amplitudes, we have been able to control the energy gaps at the center and at the border of the MBZ. Our results were verified to agree very well with both experimental and theoretical evidence found in the literature for similar structures composed of GaAs/AlGaAs.

Finally, we finish by proposing that novel structures and material combinations could arise based on this work. Two and three-dimensional optical microcavity designs would be possible, for example, or even crossing SAW beams on POMCs (i.e., two SAW beams being generated along normal in-plane directions), nanostructures could be inserted into the optical cavity for addressing light-matter couplings, etc. A very wide range of applications thus exists, and it is up to the reader to decide on what this work could be most useful.

Bibliography

[1] D. Royer and E. Dieulesaint. *Elastic waves in solids II: Generation, acousto-optic interaction, applications*. Springer-Verlag, 2000.

[2] Ahmad Safari and E. Koray Akdogan, editors. *Piezoelectric and Acoustic Materials for Transducer Applications*. Springer Science + Business Media, 2008.

[3] G. Lippmann. Principe de la conservation d'électricité. In *Annales de chimie et de physique*, volume 24, pages 145 – 178, 1881.

[4] Jacques and Pierre Curie. Contractions et dilatations produites par des tensions dans les cristaux hémièdres à faces inclinées. In *Comptes rendus hebdomadaires des séances de l'académie de sciences*, volume 93, pages 1137 – 1140, 1881.

[5] D. S. Ballantine, R. M. White, S. J. Martin, A. J. Ricco, E. T. Zellers, G. C. Frye, and H. Wohltjen. *Acoustic wave sensors: theory, design and physico-chemical applications*. Academic Press, 1997.

[6] P. V. Santos, M. Ramsteiner, and F. Jungnickel. Spatially resolved photoluminescence in GaAs surface acoustic wave structures. *Applied Physics Letters*, 72:2099, 1998.

[7] T. Sogawa, P. V. Santos, S. K. Zhang, S. Eshlaghi, A. D. Wieck, and K. H. Ploog. Transport and lifetime enhancement of photoexcited spins in GaAs by surface acoustic waves. *Physical Review Letters*, 87:276601, 2001.

[8] O. D. D. Couto, Jr., F. Iikawa, J. Rudolph, R. Hey, and P. V. Santos. Anisotropic spin transport in (110) GaAs quantum wells. *Physical Review Letters*, 98:036603, 2007.

[9] O. D. D. Couto, Jr., R. Hey, and P. V. Santos. Spin dynamics in (110) GaAs quantum wells under surface acoustic waves. *Physical Review B*, 78:153305, 2008.

[10] Sajeev John and Shengjun Yang. Electromagnetically induced exciton mobility in a photonic band gap. *Physical Review Letters*, 99:046801, 2007.

[11] J. Rudolph, R. Hey, and P. V. Santos. Long-range exciton transport by dynamic strain fields in a GaAs quantum well. *Physical Review Letters*, 99:047602, 2007.

[12] O. D. D. Couto, Jr., S. Lazic, F. Iikawa, J. A. H. Stotz, U. Jahn, R. Hey, and P. V. Santos. Photon anti-buching in acoustically pumped quantum dots. *Nature Photonics*, 3:645, 2009.

[13] Kerry J. Vahala. Optical microcavities. *Nature*, 424:839–846, 2003.

[14] T. Yoshie, A. Scherer, J. Hendrickson, G. Khitrova, H. M. Gibbs, G. Rupper, C. Ell, O. B. Shchekin, and D. G. Deppe. Vacuum rabi splitting with a single quantum dot in a photonic crystal nanocavity. *Nature*, 432:200, 2004.

[15] J. P. Reithmaier, G. Se, A. Loffler, C. Hofmann, S. Kuhn, s. Reitzenstein, L. V. Keldysh, V. D. Kulakovskii, T. L. Reinecke, and A. Forchel. Strong coupling in a single quantum dot-semiconductor microcavity system. *Nature*, 432:197, 2004.

[16] K. Hennessy, A. Badolato, M. Winger, D. Gerace, M. Atature, S. Gulde, S. Falt, E. L. Hu, and A. Imamoglu. Quantum nature of a strongly coupled single quantum dot-cavity system. *Nature*, 445:896, 2007.

[17] Grant A. Fowles. *Introduction to modern optics*. Dover Publications, second edition, 1989.

[18] C. R. Pollock and M. Lipson. *Integrated photonics*. Springer Science + Business Media, 2003.

[19] D. G. Lidzey, D. D. C. Bradley, M. S. Skolnick, T. Virgili, S. Walker, and D. M. Whittaker. Strong exciton-photon coupling in an organic semiconductor microcavity. *Nature*, 395:53, 1998.

[20] C. Dang, J. Lee, C. Breen, J. S. Steckel, S. Coe-Sullivan, and A. Nurmikko. Red, green and blue lasing enabled by single-exciton gain in colloidal quantum dot films. *Nature Nanotechnology*, 7:335, 2012.

[21] Robert J. Pressley, editor. *Handbook of Lasers with Selected Data on Optical Technology*. Chemical Rubber Co., 1971.

[22] Optical society of America. *Handbook of optics, volume II: devices, measurements and properties*. McGraw-Hill, 1995.

[23] H. Eklund, A. Roos, and S. T. Eng. Rotation of laser beam polarization in acousto-optic devices. *Optical and Quantum Electronics*, 7:73 – 79, 1975.

[24] Jr. M. M. de Lima, R. Hey, P.V. Santos, and A. Cantarero. Phonon-induced optical superlattice. *Physical Review Letters*, 94:126805, 2005.

[25] M. M. de Lima, Jr., R. Hey, J. Camacho, A. Cantarero, and P. V. Santos. Acoustically tunable photonic structures based on microcavity polaritons. *Physica E*, 32(1-2):496, 2005.

[26] E. A. Cerda-Mendez, D. N. Krizhanovskii, M. Wouters, R. Bradley, K. Biermann, K. Guda, R. Hey, P. V. Santos, D. Sarkar, and M. S. Skolnick. Polariton condensation in dynamic acoustic lattices. *Physical Review Letters*, 105:116402, 2010.

[27] M. M. de Lima, Jr. and P. V. Santos. Modulation of photonic structures by surface acoustic waves. *Reports on Progress in Physics*, 68:1639, 2005.

[28] Ivo Babuska, Uday Banerjee, and John E. Osborn. Generalized finite element methods - main ideas, results and perspective. *International Journal of Computational Methods*, 1:67 – 103, 2004.

[29] D. Royer and E. Dieulesaint. *Elastic waves in solids I: Free and guided propagation*. Springer-Verlag, 2000.

[30] J. F. Nye. *Physical properties of crystals*. Oxford University Press, 1957.

[31] Jacques and Pierre Curie. Développement par compression de l'électricité polaire dans les cristaux hémièdres à faces inclinées. In *Bulletin de la Société minérologique de France*, volume 3, pages 90 – 93, 1880.

[32] Lord Rayleigh, D. C. L., and F. R. S. On waves propagated along the plane surface of an elastic solid. In *Proc. of the London mathematical society*, volume s1-17, Issue 1, pages 4–11, 1885.

[33] K. A. Ingebrigsten. Surface waves in piezoelectrics. *Journal of Applied Physics*, 40:2681, 1969.

[34] Quing-Huo Liu and Jianping Tao. The perfectly matched layer for acoustic waves in absorptive media. *The Journal of the Acoustic Society of America*, 102:2072, 1997.

[35] X. Y. Du, Y. Q. Fu, S. C. Tan, J. K. Luo, A. J. Flewitt, W. I. Milne, D. S. Lee, N. M. Park, J. Park, Y. J. Choi, S. H. Kim, and S. Maeng. ZnO film thickness effect on surface acoustic wave modes and acoustic streaming. *Applied Physics Letters*, 93:094105, 2008.

[36] Andrew J. Slobodnik Jr. The temperature coefficients of acoustic surface wave velocity and delay on lithium niobate, lithium tantalate, quartz, and tellurium dioxide. *Physical Sciences Research Papers, N-477*, AFCRL-72-0082, 1972.

[37] Mark Fox. *Quantum Optics: An introduction*. Oxford University Press, 2006.

[38] P. D. Batista, B. Drescher, W. Seidel, J. Rudolph, S. Jiao, and P. V. Santos. ZnO/SiO_2 microcavity modulator on silicon. *Applied Physics Letters*, 92:133502, 2008.

[39] Richard P. Feynman, Matthew Sands, and Robert B. Leighton. *The Feynman lectures on Physics*, volume 1. Addison Wesley, 1977.

[40] Refractive index database. `http://refractiveindex.info/`.

Appendix A

Tables

Crystal (class)	Unit cell	Stiffness tensor
Cubic (all)	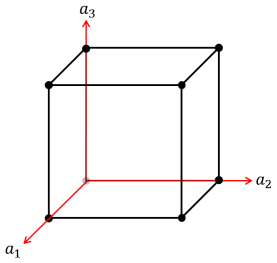	$\begin{bmatrix} c_{11} & c_{12} & c_{12} & 0 & 0 & 0 \\ c_{12} & c_{11} & c_{12} & 0 & 0 & 0 \\ c_{12} & c_{12} & c_{11} & 0 & 0 & 0 \\ 0 & 0 & 0 & c_{44} & 0 & 0 \\ 0 & 0 & 0 & 0 & c_{44} & 0 \\ 0 & 0 & 0 & 0 & 0 & c_{44} \end{bmatrix}$
Hexagonal (all)	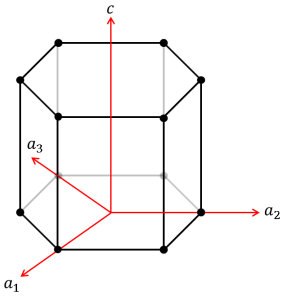	$\begin{bmatrix} c_{11} & c_{12} & c_{13} & 0 & 0 & 0 \\ c_{12} & c_{11} & c_{13} & 0 & 0 & 0 \\ c_{13} & c_{13} & c_{33} & 0 & 0 & 0 \\ 0 & 0 & 0 & c_{44} & 0 & 0 \\ 0 & 0 & 0 & 0 & c_{44} & 0 \\ 0 & 0 & 0 & 0 & 0 & \frac{c_{11}-c_{12}}{2} \end{bmatrix}$
Trigonal $(3m, 32)$	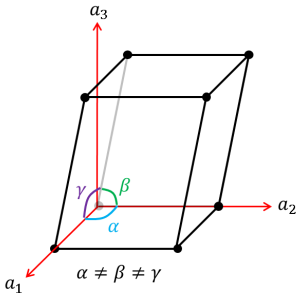	$\begin{bmatrix} c_{11} & c_{12} & c_{13} & c_{14} & 0 & 0 \\ c_{12} & c_{11} & c_{13} & -c_{14} & 0 & 0 \\ c_{13} & c_{13} & c_{33} & 0 & 0 & 0 \\ c_{14} & -c_{14} & 0 & c_{44} & 0 & 0 \\ 0 & 0 & 0 & 0 & c_{44} & c_{14} \\ 0 & 0 & 0 & 0 & c_{14} & \frac{c_{11}-c_{12}}{2} \end{bmatrix}$

Table A.1: unit cells and stiffness tensors for several crystalline structures. [29, 30]

Material	**Crystal lattice**	**Density** ($\mathbf{kg/m^3}$)	**Stiffness** ($\mathbf{10^{10}N/m^2}$)					
		ρ	c_{11}	c_{12}	c_{13}	c_{33}	c_{44}	c_{14}
Aluminium (Al)	Cubic ($m3m$)	2702	10.73	6.08	-	-	2.83	-
Gallium Arsenide (GaAs)	Cubic ($\bar{4}3m$)	5307	11.88	5.38	-	-	5.94	-
Lithium Niobate ($LiNbO_3$)	Trigonal ($3m$)	4700	20.3	5.3	7.5	24.5	6.0	0.9
α-Quartz (SiO_2)	Trigonal (32)	2648	8.67	0.7	1.19	10.72	5.79	-1.79
Sapphire (Al_2O_3)	Trigonal ($\bar{3}2m$)	3980	49.7	16.3	11.1	49.7	14.7	-2.35
Silica (SiO_2)	Cubic (*isotropic*)	2203	7.85	1.81	-	-	3.12	-
Silicon (Si)	Cubic ($m3m$)	2329	16.56	6.39	-	-	7.95	-
Zinc Oxide (ZnO)	Hexagonal ($6mm$)	5676	20.97	12.11	10.51	21.09	4.25	-

Table A.2: density and stiffness constants for several materials. [29]

Material	**Piezoelectric tensor**	**Piezoelectric constant (C/m^2)**					
		d_{11}	d_{14}	d_{15}	d_{22}	d_{31}	d_{33}
Gallium Arsenide (GaAs)	$\begin{bmatrix} 0 & 0 & 0 & d_{14} & 0 & 0 \\ 0 & 0 & 0 & 0 & d_{14} & 0 \\ 0 & 0 & 0 & 0 & 0 & d_{14} \end{bmatrix}$	-	-0.16	-	-	-	-
Lithium Niobate ($LiNbO_3$)	$\begin{bmatrix} 0 & 0 & 0 & 0 & d_{15} & -d_{22} \\ -d_{22} & d_{22} & 0 & d_{15} & 0 & 0 \\ d_{31} & d_{31} & d_{33} & 0 & 0 & 0 \end{bmatrix}$	-	-	3.7	2.5	0.2	1.3
α-Quartz (SiO_2)	$\begin{bmatrix} d_{11} & -d_{11} & 0 & d_{14} & 0 & 0 \\ 0 & 0 & 0 & 0 & -d_{14} & -d_{11} \\ 0 & 0 & 0 & 0 & 0 & 0 \end{bmatrix}$	0.171	0.041	-	-	-	-
Zinc Oxide (ZnO)	$\begin{bmatrix} 0 & 0 & 0 & 0 & d_{15} & 0 \\ 0 & 0 & 0 & d_{15} & 0 & 0 \\ d_{31} & d_{31} & d_{33} & 0 & 0 & 0 \end{bmatrix}$	-	-	-0.59	-	-0.61	1.14

Table A.3: piezoelectric tensors and constants for several materials. [29]

Material	**Relative permittivity**	**Refractive index at 800 nm**
Gallium Arsenide (GaAs)	10.989	3.683
Lithium Niobate ($LiNbO_3$)	$\begin{bmatrix} 43.934 & 0 & 0 \\ 0 & 43.934 & 0 \\ 0 & 0 & 29.026 \end{bmatrix}$	$\begin{bmatrix} 2.255 & 0 & 0 \\ 0 & 2.255 & 0 \\ 0 & 0 & 2.175 \end{bmatrix}$
Silica (SiO_2)	3.75	1.453
Zinc Oxide (ZnO)	$\begin{bmatrix} 8.335 & 0 & 0 \\ 0 & 8.335 & 0 \\ 0 & 0 & 8.843 \end{bmatrix}$	$\begin{bmatrix} 1.959 & 0 & 0 \\ 0 & 1.959 & 0 \\ 0 & 0 & 1.974 \end{bmatrix}$

Table A.4: relative permittivity and refractive index for several materials. [29, 22, 40]

Crystal symmetry (class)	Acousto-optic tensor
Cubic (all)	$\begin{bmatrix} p_{11} & p_{12} & p_{12} & 0 & 0 & 0 \\ p_{12} & p_{11} & p_{12} & 0 & 0 & 0 \\ p_{12} & p_{12} & p_{11} & 0 & 0 & 0 \\ 0 & 0 & 0 & p_{44} & 0 & 0 \\ 0 & 0 & 0 & 0 & p_{44} & 0 \\ 0 & 0 & 0 & 0 & 0 & p_{44} \end{bmatrix}$
Hexagonal (all)	$\begin{bmatrix} p_{11} & p_{12} & p_{13} & 0 & 0 & 0 \\ p_{12} & p_{11} & p_{13} & 0 & 0 & 0 \\ p_{31} & p_{31} & p_{33} & 0 & 0 & 0 \\ 0 & 0 & 0 & p_{44} & 0 & 0 \\ 0 & 0 & 0 & 0 & p_{44} & 0 \\ 0 & 0 & 0 & 0 & 0 & p_{66} \end{bmatrix}$
Trigonal ($3m$, 32)	$\begin{bmatrix} p_{11} & p_{12} & p_{13} & p_{14} & 0 & 0 \\ p_{12} & p_{11} & p_{13} & -p_{14} & 0 & 0 \\ p_{31} & p_{31} & p_{33} & 0 & 0 & 0 \\ p_{41} & -p_{41} & 0 & p_{44} & 0 & 0 \\ 0 & 0 & 0 & 0 & p_{44} & p_{41} \\ 0 & 0 & 0 & 0 & p_{14} & p_{66} \end{bmatrix}$

Table A.5: Acousto-optic tensors for several crystalline structures. [1, 22]

Constant	GaAs	SiO_2	ZnO	$LiNbO_3$
p_{11}	-0.165	0.121	0.222	0.036
p_{12}	-0.14	0.27	0.199	0.072
p_{13}	-	-	-0.111	0.092
p_{14}	-	-	-	0.07
p_{31}	-	-	0.088	0.178
p_{33}	-	-	-0.235	0.088
p_{41}	-	-	-	0.155
p_{44}	-0.072	-0.075	-0.061	-
p_{66}	-	-	0.0015	-0.018

Table A.6: Acousto-optic constants for several materials. [1, 22]

Appendix B

Stress tensor symmetry proof

We describe the local rotation of a small volume δV, with moment of inertia I_k, through an angle θ_k towards the Ox_k axis. Figure B.1 illustrates the rotation. The torque due to the traction is $\vec{r} \times \vec{T}$, which can be expressed as

$$(\vec{r} \times \vec{T})_k = \epsilon_{ijk} x_i T_j, \tag{B.1}$$

where we have used the antisymmetric tensor

$$\epsilon_{ijk} = \begin{cases} 1, & \text{if the permutation between } i,\ j \text{ and } k \text{ is even,} \\ 0, & \text{if two or three indices are equal,} \\ -1, & \text{if the permutation between } i,\ j \text{ and } k \text{ is odd.} \end{cases} \tag{B.2}$$

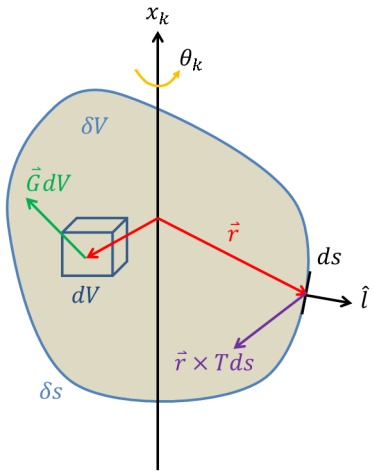

Figure B.1: a volume element δV, with surface area δs, is subjected to a rotation around the Ox_k axis due to a torque caused by the traction.

The material external to the volume δV applies tractions from every side, so that the components of the torque, M_k, are integrals over the surface δs:

$$M_k = \int_{\delta s} \epsilon_{ijk} x_i T_j ds_m. \tag{B.3}$$

Taking equation 2.16b into account, we have

$$M_k = \int_{\delta s} \epsilon_{ijk} x_i T_{jm} l_m ds. \tag{B.4}$$

We can write this surface integral as a volume integral:

$$M_k = \sum_{m=1}^{3} \int_{\delta V} \frac{(\partial \epsilon_{ijk} x_i T_{jm})}{\partial x_m} dV = \sum_{m=1}^{3} \int_{\delta V} \Big(\epsilon_{ijk} x_i \frac{\partial T_{jm}}{\partial x_m} + \epsilon_{ijk} \frac{\partial x_i}{\partial x_m} T_{jm} \Big) dV. \tag{B.5}$$

The coordinates x_i and x_m are independent, thus allowing us to write

$$M_k = \sum_{m=1}^{3} \int_{\delta V} \Big(\epsilon_{ijk} x_i \frac{\partial T_{jm}}{\partial x_m} + \epsilon_{ijk} \delta_{im} T_{jm} \Big) dV = \sum_{m=1}^{3} \int_{\delta V} \Big(\epsilon_{ijk} x_i \frac{\partial T_{jm}}{\partial x_m} + \epsilon_{ijk} T_{ji} \Big) dV. \tag{B.6}$$

If there's an external torque, with volume density G_k, then the equation of motion becomes

$$I_k \frac{\partial^2 \theta_k}{\partial t^2} = \sum_{m=1}^{3} \int_{\delta V} \Big(\epsilon_{ijk} x_i \frac{\partial T_{jm}}{\partial x_m} + \epsilon_{ijk} T_{ji} + G_k \Big) dV, \tag{B.7a}$$

where the moment of inertia is defined as

$$I_k = \int_{\delta V} \rho r^2 dV. \tag{B.7b}$$

As $\delta V \to 0$, the integrals that depend explicitly on the spatial coordinates become negligible. Thus, equation B.7a reduces to

$$\epsilon_{ijk} T_{ji} + G_k = 0, \tag{B.8}$$

which can be written as

$$T_{ji} - T_{ij} + G_k = 0. \tag{B.9}$$

In the absence of external torque ($G_k = 0$), we obtain

$$T_{ij} = T_{ji}. \tag{B.10}$$

Thus, the stress tensor is symmetric.